Polymer Chemistry

REVIEW

View Article Online
View Journal | View Issue

Cite this: *Polym. Chem.*, 2017, **8**, 4947

Multicellular tumor spheroids: a relevant 3D model for the *in vitro* preclinical investigation of polymer nanomedicines

Gianpiero Lazzari, Patrick Couvreur and Simona Mura *

The application of nanotechnology to medicine, usually termed nanomedicine, has given a crucial impulse to the design of various drug-loaded nanocarriers driven by the aim to overcome the limits associated with traditional drug delivery modalities, in particular, in the field of cancer treatment. However, an appropriate preclinical evaluation of the real therapeutic potential of nanomedicines suffers from the lack of relevant models that are well representative of the human disease and good predictors of the therapeutic response in patients. In this context, great emphasis has been directed toward 3D tumor models aiming to surmount the insufficient predictive power of traditional 2D monolayer cultures of cancer cells. This review focuses on multicellular tumor spheroids (MCTS), which are currently the most widely employed 3D tumor model in preclinical studies. After a brief discussion on spheroid construction strategies and analytical/imaging techniques employed in experimental settings, the application of 3D MCTS to the evaluation of nanomedicines displaying various physico-chemical properties is reviewed. Finally, relevant examples of scaffold and microfluidic systems in which MCTS have been included are described.

Received 3rd April 2017,
Accepted 15th May 2017

DOI: 10.1039/c7py00559h

rsc.li/polymers

1. Introduction

The efficacy of conventional therapies is often limited by a non-specific cell/tissue distribution of drugs, and their rapid metabolization and/or excretion from the body. In this context, nanoscale systems for drug delivery (*i.e.*, nanomedicines) have

Institut Galien Paris-Sud, UMR 8612, CNRS, Univ Paris-Sud, Université Paris-Saclay, Faculté de Pharmacie, 5 rue Jean-Baptiste Clément, F-92296 Châtenay-Malabry cedex, France. E-mail: simona.mura@u-psud.fr

Gianpiero Lazzari

Gianpiero Lazzari graduated in Nanobiotechnology from the University of Salento (Italy) in 2015 and then he joined the group of Prof. Patrick Couvreur (Institut Galien Paris-Sud) at the University Paris-Sud (Chatenay-Malabry, France) as a PhD researcher with a Marie Skłodowska-Curie fellowship in the framework of the NABBA project (NAnomedicines to overcome Biological BArriers and to treat severe diseases). His research focuses on the development of relevant in vitro *3D and* in vivo *models of pancreatic cancer for preclinical evaluation of nanomedicines.*

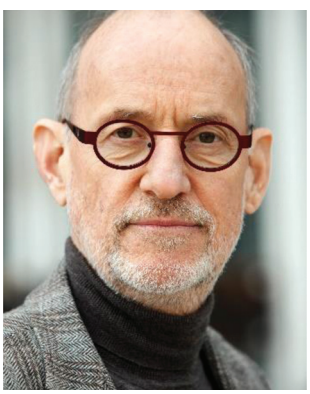

Patrick Couvreur

*Patrick Couvreur is a Full Professor of Pharmacy at the Paris-Sud University (France). He held the Innovation Technologique chair (2009–2010) at the prestigious Collège de France and received an ERC Advanced Grant (2010–2015). Patrick Couvreur's contributions in the field of nanomedicine are highly recognized and respected around the world (*H*-index 84 and over 28 000 citations). His research is interdisciplinary, being at the interface between physico-chemistry of colloids, polymer chemistry, materials science and pharmacology with applications in oncology and neurosciences. He is a member of several Academies both in France and abroad.*

received in the last few decades tremendous attention because they hold the potential to overcome these limits, providing a solution to medical challenges that urgently require novel therapeutic strategies.[1–3] Nanomedicines can indeed improve the therapeutic index of the transported drug by (i) offering protection from degradation, (ii) enabling its controlled release and distribution and (iii) increasing its bioavailability. In particular, with cancer being one of the leading causes of death worldwide, much work has been done in this field with the aim of proposing more efficient treatments.

Accordingly, a plethora of well-engineered nanomedicines surface-modified with cell targeting ligands[4] or endowed with stimuli-responsiveness[5] have been designed. However, despite the encouraging results observed in preclinical experimental models as well as in clinical trials,[6,7] the introduction of nanoscale drug delivery systems in clinical practice is not straightforward,[8,9] and only a limited number of nanomedicines have reached the marketplace. These include, for instance, lipid and natural protein-based nanomedicines such as Doxorubicin (Doxo)-loaded liposomes (*i.e.*, Doxil®, Myocet®) and paclitaxel albumin-bound nanoparticles (NPs) (*i.e.*, Abraxane®). It is noteworthy that so far no nanomedicine based on synthetic polymers has been introduced in the market despite the high versatility offered by the macromolecular synthesis and the possibility of opportunely tuning the polymers' properties (*e.g.*, composition, structure, functionalization, degradability *etc.*).[10–13]

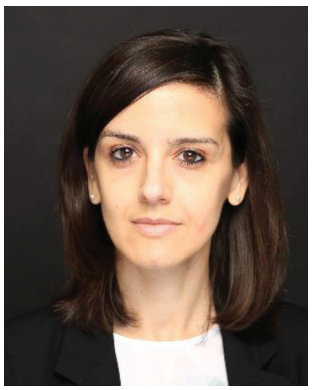

Simona Mura

Dr Simona Mura gained her degree in Pharmaceutical Chemistry and Technology in 2005. In 2009, she was awarded her PhD in Chemistry and Technology of Drugs at the University of Cagliari, Italy, working on the design and in vitro *evaluation of novel vesicular systems for the topical delivery of drugs. In 2008 she joined the group of Prof. Elias Fattal (UMR CNRS 8612) at the University Paris-Sud, Chatenay-Malabry, France, as a post-doctoral research assistant to study the lung toxicity of biodegradable nanoparticles designed for pulmonary administration of drugs. In 2011 she was appointed Associate Professor within the framework of the "CNRS-Higher Education chairs (*Chaire d'excellence*)" programme, in the group of Prof. Patrick Couvreur (UMR CNRS 8612) at the University Paris-Sud, Chatenay-Malabry, France. Her research focuses on the design of novel lipid and biopolymer-based nanoscale drug delivery systems for the treatment of severe neoplastic diseases and on the development of valuable 3D* in vitro *models for the assessment of their therapeutic efficacy.*

It has to be noted that reaching the biological targets and ensuring sufficient drug delivery and accumulation is extremely challenging as a consequence of the multiple biological barriers that characterize tumors and their microenvironment, which are crossed by nanomedicines either at low efficiency or not at all.[14,15] However, such biological transport barriers are generally not taken into account during the *in vitro* preclinical evaluation of nanomedicines, the majority of which is still routinely carried out in two dimensional (2D) monocultures of isolated cancer cells. Despite their relative ease of handling, these cultures do not show any structural architecture and lack the complex physiology and the microenvironment of real tumor tissues, which consist of different cell types (*e.g.*, fibroblasts, macrophages, endothelial cells, immune cells) embedded in an extracellular matrix (ECM) mainly composed of fibrous proteins and proteoglycans.[16–18] Cells cultured in 2D monolayers display altered gene expression and activation of signaling pathways when compared to cells grown in the native tumor tissue.[19] Moreover, growing in a single layer, they do not replicate either (i) the cell-to-cell and cell-to-ECM interactions[20–22] or (ii) the oxygen, nutrients and pH gradients,[23] which play a crucial role in tumor progression, chemoresistance and metastatic spread.[24]

Accordingly, there is an urgent need for more relevant models capable of closely mimicking the heterogeneity and the microenvironment of the *in vivo* conditions, thus allowing a more predictive *in vitro* evaluation of nanomedicines. In this context, three dimensional (3D) culture models such as multicellular spheroids (MCTS), polymer scaffolds and microfluidic systems have been proposed as an alternative approach to overcome the aforementioned limitations.[25–32]

3D tumor models are indeed capable of recapitulating some key features of real tumors, thus representing a valuable tool for (i) a more accurate preclinical screening of nanomedicines and (ii) the identification of candidates with the highest chances of success, which would be further evaluated *in vivo*. According to their predictive capacity, 3D models would enable to limit the number of animals required in preclinical studies allowing to abide by the 3Rs guidelines.[33,34]

Although the application of 3D models for a systematic assessment of the therapeutic efficacy of nanomedicines is still at the beginning, their superiority to 2D models is nowadays clearly acknowledged. This review will provide the reader with an overview of the application of multicellular tumor spheroids, the widest employed 3D tumor model so far, for the evaluation of nanomedicines, highlighting their usefulness as a discriminating tool. In agreement with the scope of the journal, attention has been focused on drug delivery systems either made of polymers or in which polymers have been used for surface modifications.

2. 3D multicellular tumor spheroids

Multicellular tumor spheroids are scaffold-free spherical self-assembled aggregates of cancer cells displaying an intermedi-

ate complexity between 2D *in vitro* cell cultures (*i.e.*, cell monolayers) and *in vivo* solid tumors with which they share important similarities. Since their first introduction in the early 1970s by Sutherland and coworkers,[35,36] the application of multicellular tumor spheroids in drug discovery has grown exponentially, offering the possibility of screening a large variety of different molecules,[37–39] and they are currently considered a suitable 3D model for drug evaluation in the oncology field.[37,40]

The physiological communication and the signaling established between cells growing in close contact make possible to reproduce in spheroids key aspects of the tumor and its microenvironment such as: (i) different cell proliferative rates, (ii) specific gene expression, (iii) deposition of ECM components, (iv) cell-to-cell and cell-to-microenvironment interactions and (v) drug resistance.[40–42] Still, one limitation of MCTS is the fact that they mimic only the avascular region of *in vivo* tumor tissues, thus leaving out relevant aspects of real tumorigenesis such as the surrounding vasculature, the immune system components and the fluid dynamics.[38,41]

Large spheroids (~400–500 μm diameter) display an internal layered cell distribution analogous to that observed in solid tumors. This is the result of mass transport limitations, which interfere with the diffusion of oxygen, nutrients and metabolic wastes through the spheroid creating specific gradients.[43,44] Accordingly, thanks to the easier access to oxygen and nutrients, highly proliferating cells are located in the external layer of spheroids and correspond to tumor cells close to capillaries *in vivo.* Conversely, quiescent cells characterize the middle layer, because cell metabolism decreases progressively with the increasing distance from the spheroid periphery. Finally, a critical situation characterizes the spheroid core in which the oxygen depletion (*i.e.*, hypoxia), the nutrient shortage and the metabolic waste accumulation result in cell necrosis (Fig. 1).[40,43–45] The organization in cell layers and the presence of diffusive gradients, acting as microenvironmental stresses, force the inner cells to a specific metabolic adaptation,[43] responsible for the observed impaired therapeutic efficacy of various anticancer drugs or drug-loaded nanocarriers.[40,46] For instance, cells in the hypoxic region are resistant to drugs which promote cellular death through reactive oxygen species, while the existence of necrotic and quiescent cells reduces the therapeutic efficacy of drugs active against the proliferating ones.[40] Another important feature of MCTS is the presence of a network of structural (*i.e.*, collagen and elastin) and adhesive (*i.e.*, fibronectin and laminin) ECM proteins embedded in a gel of glycosaminoglycans and proteoglycans.[40,42] This microenvironment acts as a regulating factor influencing cell proliferation, differentiation and tumor growth.[41,43] In addition, it closely mimics the physical barriers found in real solid tumors, which obstruct the free penetration of drugs through the whole mass.[40]

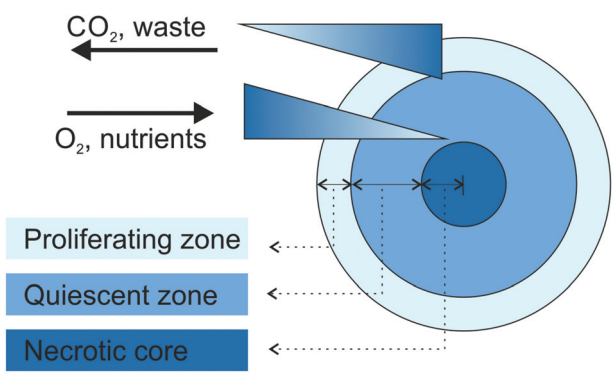

Fig. 1 Schematic representation of cell organization and gradients in tumor spheroids. Adapted with permission from ref. 44. Copyright 2008 Wiley-VCH.

Undoubtedly, the presence of this tumor microenvironment represents an advantage compared to the conventional monolayer cultures although it has to be noted that ECM components found in MCTS present a different cellular origin compared to those present in the *in vivo* tumor tissues. In the former, they are secreted by the same cancer cells forming the spheroids while in the latter they are secreted by tumor-associated fibroblasts (TAF).[42] To face this issue, spheroids composed of cancer cells and components of the supportive stroma have been recently proposed.[47,48] These hetero-type multicellular spheroids better reproduce the cellular heterogeneity of the tumor tissues and are expected to allow a more reliable evaluation of cancer cell–microenvironment interactions and their impact on the therapeutic outcomes.[43,47–49]

2.1. 3D MCTS culture methods

Different techniques for spheroid construction are currently available and many of them have been optimized for large-scale production under highly reproducible conditions.[40] Principally, they involve the use of cell attachment-resistant surfaces or physical forces to promote cell-to-cell interactions and support the 3D spheroid formation (Fig. 2). These techniques will be briefly discussed in the following paragraphs while for a more detailed and extensive description the interested reader could refer to recently published reviews.[38,41,45,50,51]

2.1.1. Liquid overlay methods. This technique mainly relies on the use of non-adherent 96-well plates, in which a coating with poly-2-hydroxyethyl methacrylate (poly-HEMA)[52–58] or agarose[59–85] prevents cell attachment. This method allows the preparation of both mono and hetero-type spheroids, whose size and morphology can be finely tuned by varying the number of cells seeded in each well.[48,50,51,86] The large number of produced spheroids and the ease of handling make this approach applicable to different kinds of high-throughput investigations.[51,86] For instance, cells could be seeded using a bulk liquid dispenser or a liquid handling robot, which also offers the possibility of scaling-up the spheroid fabrication.[37] Compared to the agitation-based approaches, the liquid overlay methods require a lower volume of media and testing materials (*e.g.*, drugs).[50,87] However, a major drawback is the time-consuming plate-coating step. Although pre-coated low cell adhesion plates are commercially

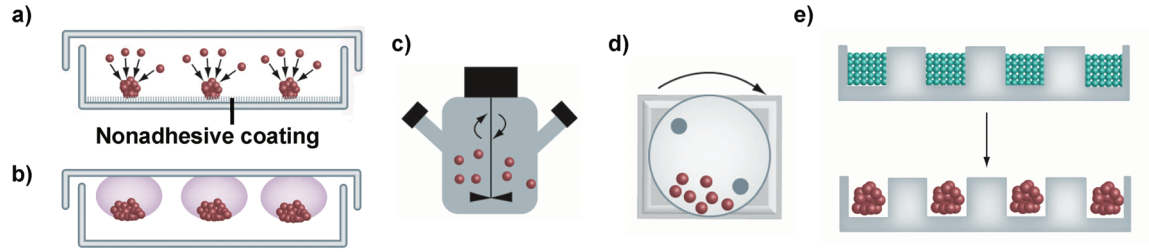

Fig. 2 Schematic representation of the main techniques used for spheroid construction: (a) liquid overlay; (b) hanging drop method; (c) spinner flask; (d) NASA bioreactor; (e) micromolding microwells. Adapted with permission from ref. 50. Copyright 2013 American Chemical Society.

available (*e.g.*, Ultra-low Attachment Surface from Corning®; PrimeSurface low adhesion culture plate from Sumitomo Bakelite Co.; Lipidure®-coated plates developed by NOF Corporation), their use increases the overall costs.[38]

2.1.2. Hanging drop methods. This technique exploits the surface tension to hang small cell suspension droplets (20–50 μL) on the underside of a tissue culture dish lid.[44,51] Then, gravity drives cell accumulation at the tip of the drop (liquid–air interface) and induces their rapid aggregation into a single spheroid.[44,50] By changing the cell density, control of spheroid size has been achieved with a high reproducibility for numerous cell lines[38] both in mono and co-cultures.[47] However, the volume of the seeding suspension is generally limited and does not provide enough nutrients for a long term culture.[44,50] Therefore, once formed, spheroids need to be transferred into 96-well plates or embedded in polymer matrices for further studies.[88–95] Not only such transfer can affect the integrity of spheroids but it clearly makes this technique extremely labor intensive and time-consuming, thus preventing large scale application.[44,50,51] Commercially available platforms (InSphero GravityPlus™ technology and PERFECTA3D™ hanging drop plates of 3D Biomatrix) can reduce the workload and enable experiments to be carried out in a high-throughput manner, although with a significant increase of the expenses.

2.1.3. Agitation-based approaches. Spinner flasks and rotational culture systems (*i.e.*, NASA Rotary Cell Culture System) are bioreactors in which cell aggregation and spheroid formation are mediated by a continuous spinning that keeps in motion a cell suspension supporting cell-to-cell interactions and avoiding their attachment to the container wall.[38] The movement of the medium provides a controlled environment and maintains the transport of nutrients and waste allowing (i) long-term culture and (ii) large-scale production. However, although by tuning the cell-seeding density, spinning rate and culture time it is possible to influence the average spheroid diameter,[44] the overall control of the number of cells per spheroid and their size is extremely poor.[38,50] Therefore, manual selection of similarly sized spheroids and their transfer into different supports are mandatory before any further assay (*e.g.*, cytotoxicity, penetration, *etc.*).[96–98]

It has to be noted that only cell lines that can withstand high shear stress can be cultured in spinner flasks.[38,50] For less resistant cells types, the NASA Rotary Cell Culture System characterized by lower shear forces, thanks to the simultaneous rotation of the culture chamber together with its content, should be instead preferred.[38,44] However, both approaches require specialized equipment and a large amount of culture media, which therefore limits their wide application.[38]

2.1.4. Patterned surfaces and microfluidic devices. Patterned surfaces in combination or not with microfluidics devices have been recently developed and offer a new range of advanced strategies for spheroid construction.[37,38,99–102] For instance, spheroids with a defined size and composition have been generated using arrays of microwells fabricated with the micromolding or the photolithography technique.[37,44,45,103,104] Low attachment surfaces have been obtained using non-adherent materials such as the poly(diméthylsiloxane) (PDMS)[46,105,106] or applying a coating of agarose[107–110] or Pluronic® F-127.[48] Compatible with traditional well plate formats and microscopes, such microwell plates are suitable for high-throughput screening.[111]

Similarly, the formation of cellular aggregates in a controlled environment and with high simplification of the liquid handling procedures has been obtained with microfluidic systems containing various micro-sized chambers and channels.[45,50,102] Requiring only limited amounts of cells, media and reagents they are extremely attractive and convenient for drug screening applications; however, the impossibility to retrieve and extensively characterize the formed spheroids is a general drawback of these approaches.[38,111] A further level of complexity is achieved with microfluidic devices displaying (i) distinct compartments loaded with different cell types (*e.g.*, epithelial cells, endothelial cells and fibroblast), (ii) collagen gel inserts and (iii) variously shaped channels, which ensure the cell-to-cell chemical communication, thus mimicking the complex *in vivo*-like organizations.[111–113] Nevertheless, to date, the complexity and the costs of the equipment required for their use have hindered their wide application in the preclinical investigation of nanomedicines.

2.2. End-point assessment in 3D MCTS

Thanks to the capacity to recreate key features of real tumors, 3D MCTS have been largely used for the assessment of the efficacy of various therapeutic strategies. In this context, assays and detection methods specific for 3D cultures are highly

required to carry out an accurate and predictive evaluation (Table 1). Their detailed description being outside the scope of this review, the most common techniques are only summarized in the next paragraphs, while a comprehensive presentation can be found in recently published articles.[37,39–41,45]

Optical microscopy is the simplest and most widely used technique for the visual assessment of morphological changes in spheroids.[52,55–58,60–65,70,73,74,77,84,89–93,95,107,110,114–126] Following exposure to various treatments, the measurement of the variation of morphometric parameters (*e.g.*, mean diameter, minimum diameter, maximum diameter, volume, area and circularity) of spheroids from bright field images is used for a quantitative analysis of the extent of growth inhibition.[37,87] After interruption of the treatment, the spheroid growth delay might be calculated in comparison with untreated samples as the time lag required to reach the quintuple spheroid volume of day 4 ($5 \times V_{d4}$; assuming V_{d4} as the starting spheroid volume at the onset of treatment).[87]

The assays currently used in 2D monolayer cultures as extensively validated methods to assess the drug cytotoxicity mainly rely on the measurement of (i) cell membrane integrity (*i.e.*, LDH assay)[127] or (ii) intracellular metabolic activity (*e.g.*, MTT, WTS-1, AlamarBlue® assays).[128] Some of them have been adapted to spheroids and are currently commercially available. Among them, the quantifications of the acid phosphatase (APH) activity and the intracellular adenosine triphosphate (ATP) level are well-suited assays that do not require preliminary dissociation of spheroids into single-cell suspensions.[37,45] The APH assay is a simple and inexpensive technique based on the quantification of cytosolic acid phosphatase activity in viable cells through the measurement of the absorption of the *p*-nitrophenol, obtained by APH hydrolyzation of *p*-nitrophenyl phosphate, at 405 nm using any standard plate detection reader.[37,129] The APH assay has been validated to measure spheroid viability and cytotoxic effects of both free drugs[87,129] and drug-loaded nanocarriers.[82,95,115,124]

The ATP assay exploits the oxidation of the luciferin, the substrate of the firefly luciferase enzymes, in the presence of O_2, Mg^{2+} and ATP. This reaction brings the luciferin to an electronically excited state, which then decays with the emission of a photon of light (*i.e.*, bioluminescence). Thus, when substrate and enzyme are added to cell cultures the light output, which is directly proportional to the intracellular ATP content (marker of metabolically active cells), allows to quantify the number of viable cells. Ready-to-use assay kits, which exploit the high sensitivity and the low background of the bioluminescence signal[45] (*e.g.*, CellTiter-Glo® 3D Cell Viability Assay (Promega); Molecular Probes® ATP Determination Kit (Invitrogen)), are currently available. The CellTiter-Glo® 3D Cell Viability Assay represents a time-effective and well standardized assay since the addition of a single reagent directly to the 3D cell culture results in cell lysis and simultaneous generation of the bioluminescence.[130] This assay is especially formulated with a robust lytic capacity to overcome 3D MCTS obstacles such as tight cell–cell junctions and the presence of the extracellular matrix.[130] The relatively simple workflow and data analysis make this ATP assay scalable to high-throughput screenings of drug-loaded nanocarrier efficacy.[125]

Qualitative assessment of proliferating or dead/necrotic cells can be performed by Confocal Laser Scanning Microscopy (CLSM) imaging following spheroid incubation with various live/dead reagents.[46,118,131] Preliminary spheroid dissociation into single cells is instead required for a quantitative measurement by Fluorescence-Activated Cell Sorting (FACS).[70] Staining cell dispersions of dissociated spheroids with fluorescently labeled Annexin V (AnnexinV-FITC) and propidium iodide (PI) has also been largely used to detect early apoptotic and dead/necrotic cells, respectively.[96,132–134] Apoptosis can be detected also on spheroid cross-sections by using the Terminal deoxynucleotidyl Transferase (TdT) dUTP Nick-End Labeling (TUNEL) method. The TdT recognition of the blunt ends of double stranded DNA breaks, which characterizes the late stages of apoptosis,[135] catalyzes the addition of biotinylated dUTPs that are then visualized using streptavidin-conjugated detection agents (*i.e.*, peroxidase or fluorescent markers).[56,136]

Monitoring of fluorescent drugs and dye-labeled nanocarriers by CLSM has been largely applied for evaluating their uptake and penetration in individual spheroids.[63,66,69,76,95,105,133] Unfortunately, compared to conventional 2D cultures, the 3D structure represents a technical challenge for conventional instrumentation. Indeed, the increases of spheroid size and thickness result in a loss of image quality due to the scattering, reflection and absorbance of light.[37,41] The layered structure of spheroids limits the inner scanning depth and, as a consequence, the penetration ability of different systems can be compared only in a portion of the spheroid generally corresponding to a depth of 80–100 μm from the spheroid surface.[63,76,95,131,137] Although more time consuming, better information on the real depth of penetration can be provided by the acquisition of fluorescent images from serial sections obtained from fixed spheroids.[46,71,88,96–98,138,139]

Compared to traditional CLSM, significant improvements in the evaluation of the penetration into living tumor spheroids can be obtained with Two-Photon (TPM) or Multi-Photon microscopy (MPM) in which the energies of two (or more) photons are combined to promote the transition of a fluorescent marker to an excited state.[140] The use of an excitation wavelength in the NIR region (700–1000 nm) offers the possibility of increasing the laser penetration into 3D MCTS (up to 500–800 μm according to the instrumentation) with low phototoxic effects.[50,140] These techniques have already been applied to visualize with high resolution the diffusion through spheroids of various polymer-based nanocarriers.[70,81,85,120,137,141] Imaging of the cellular processes and drug delivery in spheroids with an even higher 3D isotropic resolution and with limited photodamage is the promise of Light-Sheet Fluorescent Microscopy (LSFM) methods such as the Selective Plane Illumination Microscopy (SPIM)[47,142,143] method already applied for the imaging of large biological samples.[144,145] However, so far, LSFM methods have not found any application in the preclinical investigation of polymer nanomedicines.

Table 1 Methods used for the evaluation of polymer-based nanomedicines in 3D MCTS

Analyzed parameter	Assay/detection methods	Description/principle	Ref.
Cell viability/cytotoxicity	3-(4,5-Dimethyl-2-thiazolyl)-2,5-diphenyl-2*H*-tetrazolium bromide (MTT)[a,b]	Evaluation of intracellular metabolic activity Reduction of the MTT tetrazolium salt into an insoluble formazan product by the mitochondrial NADPH dehydrogenases Absorbance measurement at 570 nm	71
	2-(2-Methoxy-4-nitrophenyl)-3-(4-nitrophenyl)-5-(2,4-disulfophenyl)-2-tetrazolium (WST-1)[a,b]	Evaluation of intracellular metabolic activity Reduction of the WST-1 into a water soluble formazan product by NADH dehydrogenase and plasma membrane electron transport Absorbance measurement at 450 nm	122 and 123
	3-(4,5-Dimethylthiazol-2-yl)-5-(3-carboxymethoxyphenyl)-2-(4-sulfophenyl)-2*H*-tetrazolium (MTS)[a,b]	Evaluation of intracellular metabolic activity Reduction of the MTS tetrazolium salt into an water soluble formazan product by the mitochondrial NADPH dehydrogenases Absorbance measurement at 490 nm	65 and 88
	AlamarBlue®[a,b]	Evaluation of intracellular metabolic activity Reduction of resazurin to resorufin Fluorescence measurement. Ex 540–570 nm/Em 580–610 nm	110 and 146
	Acid phosphatase (APH)[b]	Quantification of APH activity Hydrolysis of *p*-nitrophenyl phosphate in *p*-nitrophenol by the APH enzyme Absorbance measurement at 405 nm	82, 95, 115 and 124
	Adenosine triphosphate (ATP)[b]	Measurement of the intracellular ATP content Oxidation of luciferin by the luciferase enzymes in the presence of intracellular ATP and emission of bioluminescence	66, 67, 120 and 125
	Lactate dehydrogenase (LDH)[a]	Evaluation of membrane integrity Measurement of the conversion of lactate into pyruvate *via* NAD^+ reduction by LDH. The resulting NADH catalyzes the reduction of a tetrazolium salt to a formazan product Absorbance measurement at 450 nm	53 and 136
	DNA quantification[a]	Quantification of total cell number Hoechst 33258 staining Fluorescence measurement following lyophilization and lysis of spheroids	90 and 91
Growth inhibition	Optical microscopy[c]	Measurement of morphometric parameters (*e.g.*, mean diameter, minimum diameter, maximum diameter, volume, area and circularity)	52, 55–58, 60–65, 70, 73, 74, 77, 84, 89–93, 95, 107, 110 and 114–126
Morphological effects	Scanning electron microscopy (SEM)[c]	Assessment of spheroid integrity	46, 55, 57, 63, 64, 70 and 73
Cell death/apoptosis	Trypan Blue exclusion[a]	Quantification of living cells Trypan Blue staining of dead cells	46, 70, 118, 126 and 131
	Live/dead staining	Identification and quantification of live and dead cells Staining with calcein-acetoxymethyl (calcein-AM) and intercalating agents (*e.g.*, propidium iodide (PI) or ethidium homodimer (EthD-1)). Live cells are stained in green following intracellular cleavage of the acetomethoxy group of calcein-AM. Dead cells are stained in red following penetration of the intercalating agents through their permeable membrane	46, 70, 118 and 133
	AnnexinV-FITC staining	Detection of the apoptosis marker phosphatidyl serine on the cell membrane surface with Annexin V-FITC. Used in combination with PI staining to distinguish apoptotic and necrotic cells	96, 133 and 134

Table 1 *(Contd.)*

Analyzed parameter	Assay/detection methods	Description/principle	Ref.
	Caspase-3 activation	Quantification of caspase-3 activity *via* measurement of fluorescent emission of activate-caspase-3 substrates	54 and 118
	Terminal deoxynucleotidyl transferase (TdT) dUTP Nick-End Labeling (TUNEL)	Quantification of DNA fragmentation as a marker of late apoptosis. Detection of double stranded DNA breaks *via* TdT-mediated incorporation of labeled dUTP to their blunt ends	56 and 136
Penetration/uptake of fluorescently labeled nanocarriers and dyes	Confocal Laser Scanning Microscopy (CLSM)[c]	Imaging of nanocarrier diffusion ability Pinhole-equipped microscope to remove out-of-focus light and increase optical resolution Light penetration depth limited to 100–150 μm from the spheroid surface	48, 53–60, 62–64, 66–69, 72, 74–76, 78–80, 83, 84, 89–91, 94, 95, 105–109, 115, 117–119, 122–126, 131, 133, 134, 136, 137 and 146–157
	Two-photon microscopy (TPM) and multi-photon microscopy (MPM)[c]	Imaging of nanocarrier diffusion ability Sample excitation with pulsed long-wavelength photons Increase of the image resolution and depth of penetration (up to 500–800 μm)	70, 81, 85, 120, 137 and 141
	Fluorescence-activated cell sorting (FACS)[a]	Quantification of cell fluorescence	71, 78, 85, 122, 134 and 136
	Fluorescence microscopy	Imaging of nanocarrier diffusion ability Imaging of fixed, optimal cutting temperature (O.C.T.)-embedded spheroids cross-sections	46, 71, 88, 96–98, 138 and 139

[a] Preliminary cell dissociation required. [b] Quantification of metabolically active cells. [c] Imaging of intact spheroids.

2.3. Use of 3D MCTS to screen polymer nanocarriers with different physico-chemical properties

The distinguishing characteristics of polymer nanocarriers, such as chemical composition, size, shape and surface properties, might strongly affect their capacity to diffuse into tumors and therefore have a profound impact on their anticancer efficacy.[158] Accordingly, these parameters must be taken into account during the design and evaluation of any novel nanomedicine. In this context the 3D MCTS, thanks to their similarity in morphology and biological microenvironment to solid tumors, have already been used as a robust tool for easy polymer nanoparticle screening,[70,97] and to accurately predict the *in vivo* behavior of the nanocarriers as a function of their specific physico-chemical properties.[139] The most relevant results will be discussed in the following sections.

2.3.1. The size effect. The influence of size on the penetration profile of nanoscale systems has been clearly highlighted and, according to the general trend observed *in vitro* with 3D MCTS and further confirmed *in vivo*, it is evident that the diffusion capacity is inversely correlated to the particle size.[56,72,97,98,139,148] For instance, nanogels obtained by chelating ligand-modified hyaluronic acid were capable of deeper penetration into MKN74 gastric cancer spheroids compared to the polymer in the linear form and their small size (21 nm) ensured a uniform distribution over the entire 3D mass.[106] Similarly, following release from poly(ethylene glycol) (PEG)-poly(D,L-lactide) (PLA) nanoparticles, into which they have been loaded, small polyamidoamine (PAMAM) dendrimers (G2, 2 nm) penetrated efficiently into the core of KB papilloma cell spheroids (diameter ~50 μm) as compared to their larger counterparts (G4 (5 nm) and G7 (7 nm)) whose florescent signal was detected only in the peripheral rim.[72] It is noteworthy that the size plays a major role in the capacity of tumor penetration even in the case of surface functionalization with specific ligands. By using a murine breast cancer MCTS model (4T1 cells) it was observed that RGD functionalization endowed Pluronic F127-coated paclitaxel (Ptx) nanocrystals with a better penetration ability compared to the free drug (Taxol) and to the non-functionalized carriers. However, for nanocrystals displaying similar functionalization, a smaller size (10 nm *vs.* 70 nm) conferred a greater advantage in terms of depth of penetration (Fig. 3a).[56] It has to be noted that no difference was observed when the particles were evaluated on a 2D culture model, thus highlighting the usefulness of the 3D MCTS to discern the crucial role of the size. TUNEL staining of the spheroid's cross-sections revealed that deeper penetration was associated with a more extensive cell apoptosis, which caused inhibition of spheroid growth and their further collapse following prolonged drug exposure (Fig. 3b and c).[56]

Despite these results, the identification *in vitro* of the optimal size of a nanocarrier for achieving the highest drug delivery *in vivo* is extremely complex because although MCTS closely mimic the tumor tissues, they lack predictive value in terms of pharmacokinetics and biodistribution. Accordingly, the evaluation of nanomedicines in animal tumor models still remains a mandatory step to assess these parameters. It has indeed been shown that the requirements for tumor penetration and tumor retention are often in contradiction with each other. Thus, despite being unfavorable for pene-

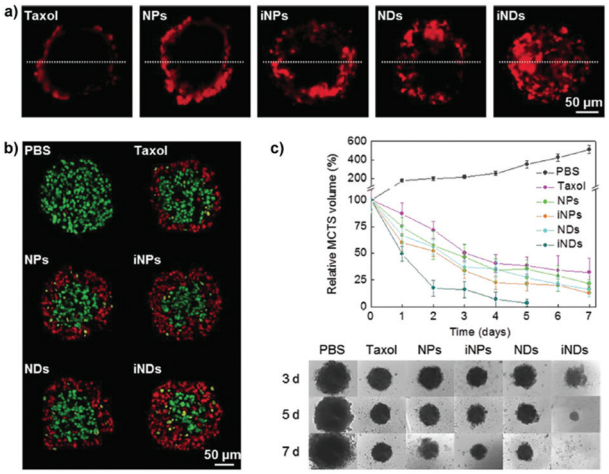

Fig. 3 Tissue penetration and antitumor efficacy in 4T1 MCTS of Taxol, ~70 nm Ptx nanocrystals (NPs), RGD-grafted ~70 nm Ptx nanocrystals (iNPs), ~10 nm Ptx nanocrystals (NDs) and RGD-grafted ~10 nm Ptx nanocrystals (iNDs). (a) CLSM images after 24 h incubation with Cy5-labeled Taxol/NDs/NPs/iNDs/iNPs, (b) CLSM images of TUNEL analysis after 24 h treatment with the different Ptx formulations; dead cells are shown in red and live cells appear in green. (c) Growth inhibitory effect of the different formulations. Reproduced with permission from ref. 56. Copyright 2015 Wiley-VCH.

tration in the tumor mass, due to their considerable diffusional hindrance,[159] nanocarriers with a size of around 100 nm are the most advantageous in improving pharmacokinetics and extravasation.[160] On the other hand, smaller nanocarriers show much better penetration in the tumor interstitial space.[139,148] However, for extremely small particles (≤5.5 nm), rapid clearance from tumors and short half-life have been observed.[161] To face this issue, the ideal drug delivery system should be able to shrink and adapt its size in response to the encountered microenvironment. Interestingly, size-switchable stimuli-responsive nanoparticles able to overcome multiple tumor barriers have been developed by various groups.[58,76,119,133,134,138,141] For instance, pH sensitive nanoparticles were formulated by the molecular assembly of platinum (PtIV)-prodrug conjugated polyamidoamine (PAMAM) dendrimers with two amphiphilic polymers containing either ionizable pH-responsive amide bonds (*i.e.*, polycaprolactone-2-propionic-3-methylmaleic anhydride (PCL-CDM), PCL-CDM-PAMAM/Pt nanoparticles)[134] or tertiary amine groups (*i.e.*, poly(ethylene glycol)-*b*-poly(2-azepane ethyl methacrylate) (PEG-*b*-PAEMA) PEG-*b*-PAEMA-PAMAM/Pt) (Fig. 4a).[133] Size variation as a function of pH has been evaluated on pancreatic cancer multicellular spheroids (BxPC3 cells). At physiological pH the clustered nanoparticles (*i.e.*, pH-sensitive cluster nanobombs (SCNs/Pt)) displayed a size of around 100 nm, while the pH drop (from 7.4 to 6.5–7) in the tumor extracellular space triggered an instantaneous disassembly of these pH sensitive nanoparticles in small Pt-PAMAM prodrugs (≈5 nm) able to penetrate deeply and uniformly into the spheroid mass (Fig. 4b). Then, once internalized, the intracellular redox environment led to the release of the active

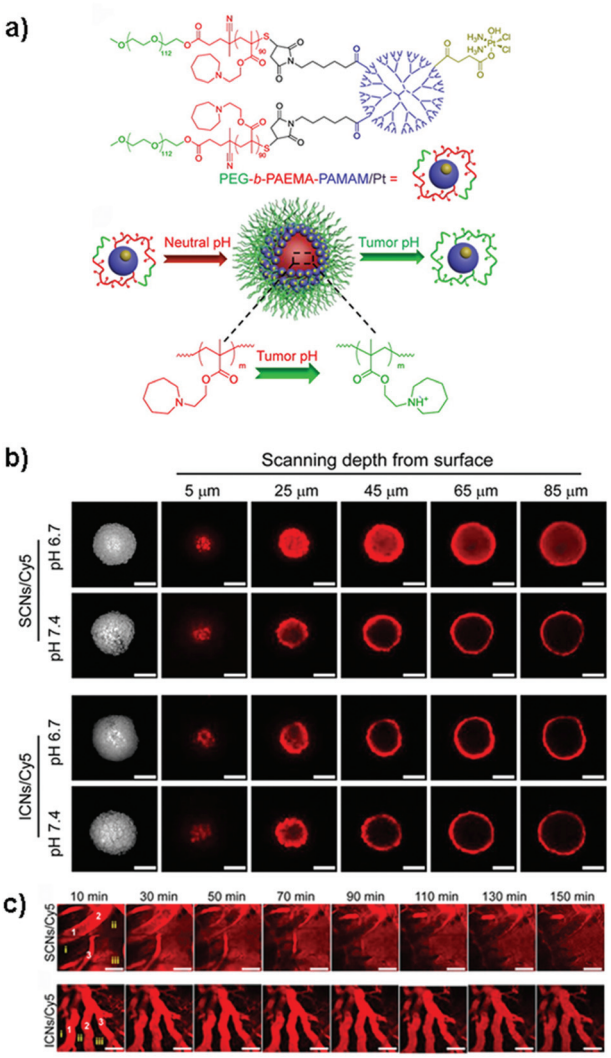

Fig. 4 (a) Structure of PEG-*b*-PAEMA-PAMAM/Pt and schematic illustration showing the self-assembly into the pH-sensitive cluster nanobombs (SCNs/Pt) at neutral pH and the disintegration into small particles at tumor acidic pH. (b) CLSM images showing *in vitro* penetration of fluorescently-labeled SCNs/Cy5 and ICNs/Cy5 in BxPC-3 multicellular spheroids. Scale bar: 100 μm. (c) *In vivo* real-time microdistribution of SCNs/Cy5 and ICNs/Cy5 in BxPC-3 xenografts after intravenous administration. Scale bar: 100 μm. Reproduced with permission from ref. 133. Copyright 2016 American Chemical Society.

molecule (*i.e.*, Pt(II) species) resulting in significant cell apoptosis. As expected, a higher cell viability was observed when spheroids were incubated with pH-insensitive nanoparticles (*i.e.*, ICNs), which demonstrated a limited capacity of penetration and drug delivery as a consequence of their stable size (Fig. 4b). Whether such advantage was maintained *in vivo* was then assessed after an intravenous injection of both nanoparticles in an experimental model of pancreatic cancer (BxPC3 cancer cells) characterized by an important desmoplastic reaction and a limited permeability.[162] Tumor accumulation studies confirmed a higher capacity of penetration of pH-sensitive nanoparticles, which diffused in the tumor inter-

stitium, after vessel extravasation, for several hundreds of nanometers. In contrast, the pH-insensitive NPs accumulated in the tumor vessels with little penetration in the tumor mass (Fig. 4c) leading to an inefficient drug delivery. In agreement with the *in vitro* results, an extensive apoptosis was detected in tumor sections of mice treated with the pH-sensitive nanoparticles, thus confirming the predictive potential of the 3D multicellular spheroids.

2.3.2. The shape effect. 3D tumor spheroids have found application also in the early screening of nanocarriers with different shapes (*i.e.*, spherical *vs.* elongated such as filaments, rod-like or worm-like vectors). However, whether this parameter may positively or negatively affect the nanocarrier penetration, the cellular uptake and the therapeutic efficacy still remains a matter of debate.[85,120,147] For instance, when worm-like poly(ethylene oxide-*b*-ε-caprolactone) (PEO-PCL) photosensitizer-loaded micelles were compared to spherical ones in 3D models of colon (HCT-116 cells) and head and neck cancer (FaDu cells), surprisingly no advantage in terms of photodynamic therapy efficiency was observed, in contradiction with the previously reported superior uptake of so-called "filomicelles".[163] Nevertheless, the different size of the studied systems, as well as other parameters such as the nanocarrier length, rigidity and surface properties, might explain such differences and would have to be further explored.[120]

The influence of length was studied by Stenzel and coworkers, who investigated rod-shaped poly(1-O-methacryloyl-β-D-fructopyranose)-*b*-poly-(methyl methacrylate) (poly(1-O-MAFru)-*b*-PMMA)-based micelles, clearly showing that, among the various fructose-coated rod-like micelles, the shortest ones displayed the highest capacity of penetration in a 3D MCTS model of breast cancer cells (MCF-7).[147] Similarly, in order to better highlight the role of these parameters, poly (ethylene glycol) diacrylate (PEGDA)-based anionic nanohydrogels were synthesized by jet and flash imprint lithography in the form of disc-shaped nanocylinders and cuboidal nanorods of two different sizes (low and high aspect ratio; aspect ratio (H/D) = height/diameter).[85] The resulting nanohydrogels displayed negative charge of ~−55 mV, which should limit the interactions with cell membranes and serum proteins and promote their penetration into HEK293 spheroids (human embryonic kidney cells). Fluorescence intensity analysis of two-photon microscopy images revealed two fold higher accumulation near the spheroid outer half of the disc-shaped nanocylinders with the lowest aspect ratio (H/D ~0.3, 325 nm diameter and 100 nm height) (Fig. 5f) compared to both nano-

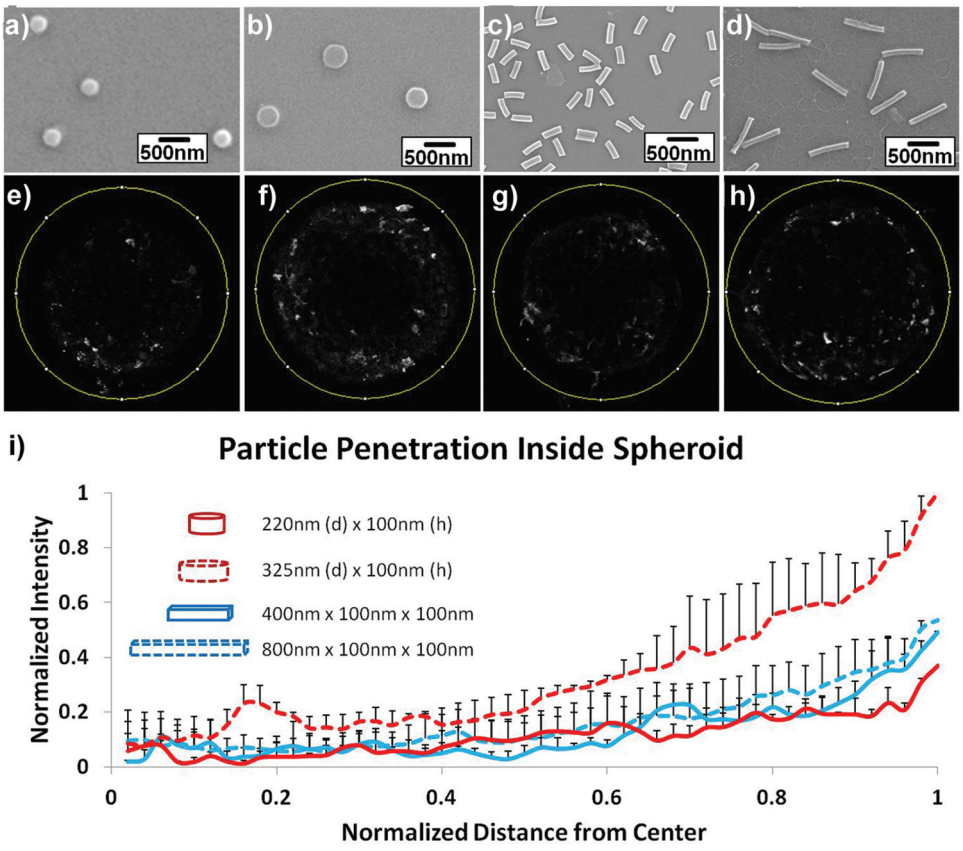

Fig. 5 Uptake and penetration of shape specific particles in spheroids. Scanning Electron Microscopy (SEM) images of (a) 220 nm × 100 nm discs (H/D ~ 0.45), (b) 325 nm × 100 nm discs (H/D ~ 0.3), (c) 400 nm × 100 nm × 100 nm rods and (d) 800 nm × 100 nm × 100 nm rods. (e–h) Two-photon pictures of spheroids incubated with the discs or rods in the correspondent upper panel. (i) Normalized radial intensity distribution as a function of distance from the center of the spheroid. Reproduced with permission from ref. 85. Copyright 2015 Wiley-VCH.

cylinders with higher aspect ratio (H/D ~0.45) (Fig. 5e) and nanorods (Fig. 5g and h). Such a preferential penetration might be attributed to their larger surface contact area, which promoted the interaction with the cells and the diffusion (either passive or active) across the 3D tumor mass.

2.3.3. The charge effect. As observed for shape and size, the surface charge of the nanocarriers might also affect tissue penetration and efficient drug delivery.[72,82,164,165] For instance, the penetrating capacities of PAMAM dendrimers were discriminated according to their size (see section 2.3.1), but also a charge effect was clearly observed showing that only the amino-modified (positively-charged) ones were capable of significant accumulation in the outer layers of breast cancer (MCF7 cells) tumor spheroids while negatively and neutral ones were completely excluded (Fig. 6a).[72] It is noteworthy that small G2-NH2 dendrimers penetrated deeper than the larger G7-NH2 ones (214 ± 36 μm *vs.* 81 ± 8.31 μm), but surface accumulation was directly proportional to the dendrimer generation (G7 > G2) and therefore to the surface charge density (*i.e.*, number of NH2 groups) (Fig. 6b). This behavior was correlated to the different strength of dendrimer–cell interactions: while it was negligible for the G2 dendrimers leading to low accumulation and fast penetration by paracellular diffusion, the firmer interaction of G7 ones led to a strong uptake, which however translated to a low diffusion *via* a transcellular mechanism.

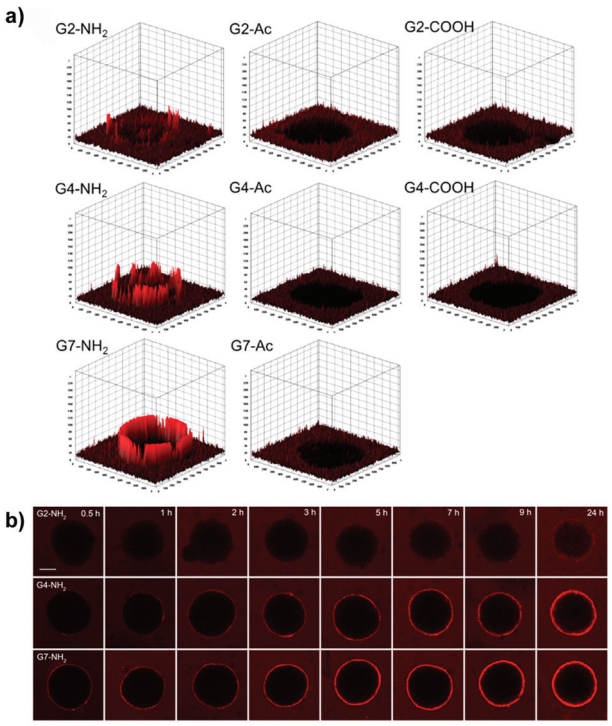

Fig. 6 (a) Accumulation and permeation behaviors of G2, G4, and G7 PAMAM dendrimers in MCF-7 MCTS as a function of the surface charge. (b) Tumor penetration of amine-terminated G2, G4, and G7 PAMAM dendrimers. Reproduced with permission from ref. 72. Copyright 2016 American Chemical Society.

The key role of a positive surface charge in the accumulation into multicellular spheroids has been shown also by comparing gold nanorods (AuNRs) (55 nm length × 14 nm diameter) coated with either (i) cetyltrimethylammonium bromide (CTAB) and poly(diallyldimethylammonium chloride) (PDDAC), or (ii) polystyrene sulfonate (PSS) displaying a surface charge of +40–50 mV or −25 mV, respectively.[82] When incubated with MCF-7 breast cancer MCTS, the coating with a cationic polymer ensured the highest gold accumulation, which was expected to induce strong photothermal cytotoxicity after NIR irradiation as was observed in 2D monolayer cultures. However, despite their tendency to be largely retained, irradiation of these positively charged AuNRs led to a 40% lower hyperthermia efficacy compared to the negatively charged PSS-coated AuNRs. Such unexpected behavior was related to the penetration capacities of the different AuNRs. Indeed, cationic polymer-coated AuNRs highly accumulated in the spheroids but only in the outer region, and simple surface adsorption was also observed. Moreover, the interaction with negatively-charged serum proteins led to an increase of their size, preventing diffusion. In contrast, the negative charge of PSS-coated AuNRs allowed a more homogeneous distribution in the spheroid core, which resulted in higher viability loss and destruction of the inner compact spheroid structure.

2.3.4. The role of the chemical composition. 3D multicellular spheroids have been used to discern whether the chemical composition of the polymer building blocks could affect the drug delivery efficacy of the resulting nanoparticles.[60,91,96,152,153,155] Thus, curcumin-loaded biodegradable and non-biodegradable nanoparticles prepared by self-assembly of bovine serum albumin (BSA) conjugated with poly-(ε-caprolactone) (PCL) or poly(methyl methacrylate) (PMMA) were investigated in LNCaP prostate cancer MCTS in comparison with conventional 2D cultures.[91] The latter did not reveal appreciable differences between the two types of nanoparticles, which were both rapidly taken up by cells and induced similar cytotoxicity. In contrast, the MTCS allowed the detection of the faster and deeper accumulation of BSA-PMMA NPs, which occurred *via* a rapid sequence of endo and exocytosis events. However, such a high penetration rate hindered sufficient intracellular drug release, thus leading to a lower cytotoxicity compared to the BSA-PCL NP, whose biodegradability ensured, in contrast, high intracellular drug concentrations (Fig. 7a). Non-biodegradable BSA-PMMA NPs induced a growth inhibition comparable to the biodegradable NPs, only when tested at 5 times higher drug concentration (Fig. 7b).

Other examples of anticancer drug-loaded biodegradable nanocarriers evaluated on 3D spheroids included milk protein nanoparticles[153] and micelles composed of either (i) pseudo block copolymers formed by the assembly of β-cyclodextrin terminated multiarmed poly(*N*-vinylpyrrolidone) (PVP) and adamantane functionalized polycaprolactone (PCL)[155] or (ii) poly (ethylene oxide)-poly [(*R*)-3-hydroxybutyrate]-poly (ethylene oxide) triblock copolymers.[96] The capacity of penetration of

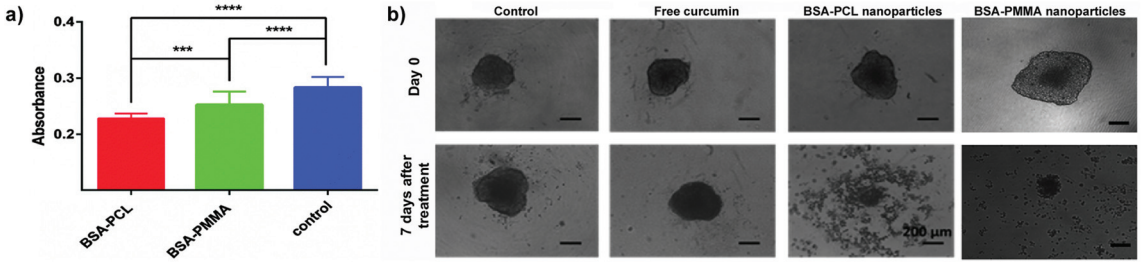

Fig. 7 (a) Absorbance values (mean ± standard error) corresponding to the DNA content in LNCaP spheroids treated with curcumin-loaded nanoparticles for 7 days. (Curcumin concentration: 30 μM.) ***$p < 0.001$. ****$p < 0.0001$. (b) LNCaP spheroids treated with free curcumin and curcumin-loaded nanoparticles for 7 days. (Curcumin concentration: 150 μM.) Scale bars: 200 μm. Reproduced with permission from ref. 91. Copyright 2016 Royal Society of Chemistry.

these nanosystems in 3D models was consistent with further *in vivo* experiments, thus supporting the predictive capacity of the tumor spheroids.[96,153,155]

2.3.5. The role of crosslinking. The capacity of amphiphilic block copolymers to self-assemble in water as micelles has been largely applied in efficient drug delivery.[90,120,167,124,166] Micelles display a typical core–shell structure and a variety of crosslinking strategies have been proposed to reach a higher stability. For instance, the irreversible crosslinking of poly(ethylene glycol methyl ether acrylate)-*b*-poly(carboxyethyl acrylate) (POEGMEA-*b*-PCEA) micelles with 1,8-diaminooctane[90,124] protected against disassembly, leading to better cellular uptake when compared to uncrosslinked counterparts. However, such a crosslink induced a reduction of the drug release, leading to micelles with lower cytotoxicity compared to the free drugs when evaluated on 2D monolayer cell cultures of human prostate carcinoma (LNCaP cells).[124] Analogous results have been obtained when glycol dimethacrylate (EGDMA) crosslinked poly(ethyleneoxide-*b*-3-caprolactone) (PEO-PCL) micelles have been investigated on HCT-116 (human colorectal carcinoma) and FaDu cells (human squamous cell carcinoma).[120] In contrast, the aforementioned micelles were characterized by superior antitumor activities to the free drug in different MCTS made with HCT-116, FaDu or LNCaP cells,[120,124] clearly demonstrating the limited predictive potential of 2D cultures in the assessment of the real value of nanocarriers as drug delivery systems.

Whether the crosslink could affect the mechanism and depth of penetration as well as the cytotoxicity of drug-loaded micelles has been recently investigated by the group of Stenzel using pancreatic (AsPc-1 cells) multicellular tumor spheroids.[90] Hence, 1,8-diaminooctane-crosslinked poly(*N*-(2-hydroxypropyl) methacrylamide-*co*-methacrylic acid)-*block*-poly(methyl methacrylate) (P(HPMA-*co*-MAA)-*b*-PMMA) micelles (CKM) were compared to their uncrosslinked version (UCM) (Fig. 8a). Results revealed that CKM were capable of moving through the cell layers *via* a transcellular process and delivered higher doxorubicin amounts to the spheroid core which resulted in greater cytotoxicity compared to the UCM (Fig. 8b–d). The latter quickly disassembled after penetration into the cells of the outer layers, releasing the loaded drug and causing

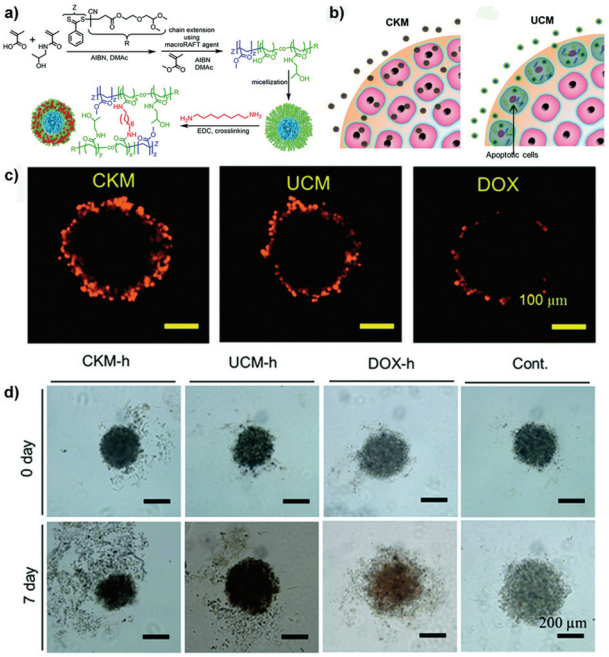

Fig. 8 (a) Schematic representation of the synthesis of block copolymer and formation of UCM and CKM. (b) Schematic hypothesis of penetration differences for Doxo-loaded CKM and UCM. (c) Doxo delivery into pancreatic MCTS by CKM and UCM revealed by CLSM. (d) Inhibition of the pancreatic MCTS growth by Doxo-loaded micelles. Microphotographs of pancreatic spheroids before and after treatment with Doxo-loaded micelles, free drug (Doxo-h) or untreated (Cont). Reproduced with permission from ref. 90. Copyright 2015 Royal Society of Chemistry.

cell death. As a result, no further micelle transcytosis could occur. The lower efficacy of the free drug (evaluated in terms of DNA content and inhibition of spheroid growth) correlated with its limited diffusion.[90]

Nevertheless, crosslinking is not always the best strategy to improve drug cytotoxicity. Thus, the evaluation of the effect of the reversible disulfide core-crosslinker cystamine in micelles formed by the poly(ethylene glycol methyl ether acrylate)-*b*-poly(carboxyethyl acrylate) (POEGMEA-*b*-PCEA) block copolymer[95] led to results that were in clear contrast to those

previously published by the same group of Stenzel.[90,124] Indeed, micelles with the highest level of crosslinking were capable of the deepest penetration in LNCaP prostate multicellular tumor spheroids, but displayed the lowest cytotoxicity. This behavior could be explained by their too compact structure that hindered intracellular reductive agents (*e.g.*, glutathione) from diffusing in the core of the micelles, thus slowing down cross-linked micelle disassembly and release of the loaded drug.[95] Compared to the 2D monolayer cultures, the 3D spheroid model would provide a reliable correlation between micelle penetration and cytotoxicity, thus allowing figuring out the real contribution of the crosslinking in terms of drug delivery efficiency.

2.3.6. The role of targeting ligands. Functionalization of the polymer nanocarrier surface with various ligands has been largely exploited as a strategy for selective cell targeting.[4] As discussed in the following sections, MCTS are currently widely used in order to assess the effectiveness of such modifications and evaluate the tumoral behavior of targeted nanoparticles.

2.3.6.1. Transferrin-targeted nanocarriers. Overexpression of transferrin receptor (TfR) has been detected in different types of rapidly proliferating tumors.[168] Accordingly, opportune surface functionalization with transferrin (Tf) has been applied to efficiently deliver drugs to cancer cells. Such modification clearly enhanced the cellular uptake and penetration depth of polyethylene glycol-phosphatidyl ethanolamine (PEG-PE) micelles[67,68] and poly(amidoamine) (PAMAM) dendrimers[61] in MCTS models of ovarian carcinoma[67,68] and glioma[61] compared to the non-functionalized counterparts. More efficient delivery of the loaded drugs (paclitaxel (Ptx)[67,68] or doxorubicin (Doxo))[61] resulted in a significant inhibition of cell proliferation confirmed by reduction of spheroid volume and metabolic activity (ATP content). A 6-fold reduction of the IC_{50} value (8.92 μM *vs.* 1.35 μM) was measured on the 3D spheroids incubated with Tf-functionalized Ptx-loaded PEG-PE micelles (as compared to non-targeted ones) but these values were higher than those observed in 2D monolayers. These results reflect a reduction of efficacy due to the existence in the MCTS of physical barriers to diffusion and a different cell sensitivity due to the 3D spatial organization.[67]

Reflectance confocal microscopy and synchrotron X-ray fluorescence microscopy (XFM) have been used to monitor, in a quantitative and qualitative manner, the capacity of penetration into 3D breast cancer spheroids (MCF-7 cells) of transferrin-decorated polymer-modified gold nanoparticles (100 nm).[105] Images revealed that although functionalization with human Tf increased the amount of internalized NPs compared to controls (*i.e.*, bovine transferrin functionalized particles and naked ones), after 48 h the penetration of functionalized NPs was limited to a depth of 50 μm, thus representing a real issue for further therapeutic applications due to their incapacity to diffuse in the tumor core.[105]

2.3.6.2. Folic acid-targeted nanocarriers. As previously observed for the transferrin receptor, also the folate receptor is largely expressed in cancer cells, thus making the functionalization with folic acid (FA) a widely applied approach to enhance the ligand-mediated uptake by cancer cells.[55,57,94,107] 3D tumor spheroids have been employed to assess the influence of the folic acid density at the NP surface on the cell targeting capacity, internalization and tumor penetration of polymer/DNA complexes (polyplexes) made by the assembly of DNA with poly(amidoamine)-poly(ethylenimine) (PME) copolymers conjugated to FA functionalized PEG (PME-(PEG-FA)). FA functionalization should enable overcoming the reduction of cellular uptake caused by the PEG chains (the so-called PEG-dilemma)[169] and make these systems valuable tools for efficient gene delivery. Divalent modification (PME-$(PEG_{3.4k}$-$FA_2)_{1.72}$) resulted in a higher receptor mediated uptake and a better penetration in HEK293 T human embryonic kidney spheroids compared to mono-functionalized (PME-$(PEG_{3.4k}$-$FA_1)_{1.66}$) and non-functionalized nanocarriers (PME-$(PEG_{3.5k})_{1.69}$) (Fig. 9a–c).[94] Indeed, although all polyplexes were detected up to 380 μm depth, the divalent FA modification allowed achieving a better cell internalization (Fig. 9d).

The *in vitro–in vivo* predictive capacity of the 3D models in the evaluation of the FA functionalized nanocarriers was recently reported. Indeed, the higher capacity of penetration *in vitro* into 3D neuroblastoma spheroids (SH-SY5Y cells) of FA-decorated Doxo-loaded soy protein NPs (SP-NPs)[55] or carboxymethyl chitosan-*N*-3-acrylamidophenylboronic acid (CMCS-PAPBA)[57] NPs resulted in the highest inhibition of tumor growth in H22 tumor-bearing mice.

2.3.6.3. Carbohydrate-targeted nanocarriers. The natural affinity of dextran for highly glycosylated surfaces has been

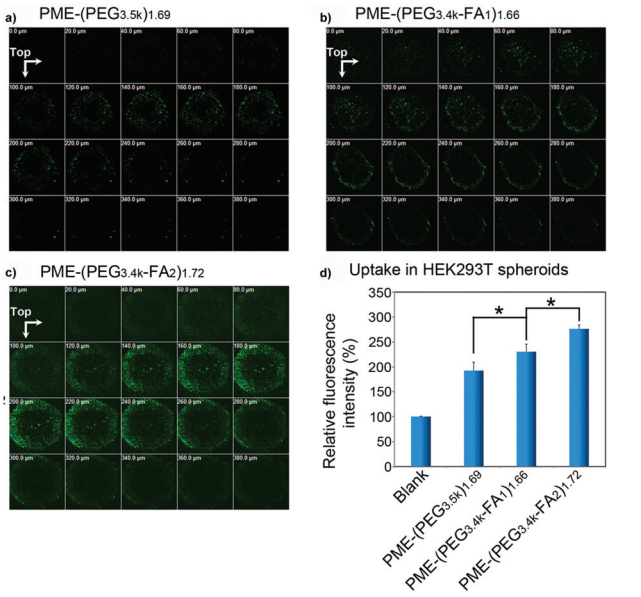

Fig. 9 CLSM images of HEK293T multicellular spheroids 22 h after transfection with (a) PME-$(PEG_{3.5k})_{1.69}$; (b) PME-$(PEG_{3.4k}$-$FA_1)_{1.66}$, or (c) PME-$(PEG_{3.4k}$-$FA_2)_{1.72}$ complexes. (d) Relative fluorescence intensity (treated group/blank) of HEK293T multicellular spheroids treated with PME-$(PEG_{3.5k})_{1.69}$, PME-$(PEG_{3.4k}$-$FA_1)_{1.66}$, or PME-$(PEG_{3.4k}$-$FA_2)_{1.72}$ complexes for 4 h and for a further 18 h culture. Reproduced with permission from ref. 94. Copyright 2015 American Chemical Society.

exploited for achieving targeted delivery of ald-dex-Doxo nanoparticles (*i.e.*, aldehyde-dextran polymer conjugated to doxorubicin *via* a pH sensitive bond) to SK-N-BE(2) cells by the interaction with the glycocalyx at their surface.[126] Investigation of these NPs in 3D neuroblastoma spheroids (~400–500 μm) enabled to discern their potential as drug delivery systems, while it was not evident under 2D conditions where the free drug displayed superior cytotoxicity. Such a difference disappeared in the spheroid model in which a drastic reduction of the free Doxo efficacy was observed while that of the ald-dex-Doxo nanoparticles remained unvaried and resulted in a more efficient reduction of tumor outgrowth. Such a difference was related to the different capacity to overcome the encountered biological barriers: after 24 h the free Doxo penetrated up to 50 μm in the spheroids while nanoparticles were detected at that depth after 1 h only and diffused in the whole mass at 4 h. Interestingly, such a capacity was exclusive of ald-dex-Doxo nanoparticles and was not observed when cells were incubated with dextran based NPs in which the drug has been only physically loaded and not covalently linked to the polymer.

Chitosan has been instead used in the formulation of nanoparticles for specific targeting of the CD44 receptor in cancer stem-like cells (CSLCs),[53,60,77,89,106,122] a rare tumor cell population whose resistance to therapeutic agents is a major cause of anticancer treatment failure.[170] While non-stem cancer cell resistance in 2D cultures is mainly the result of the overexpression of transmembrane P-glycoprotein transporters,[171] in CSLCs a key role is played also by the tumor microenvironment.[172] Accordingly, relevant preclinical investigations of such functionalized nanocarriers required a model capable of mimicking the complex relationship between cancer cells and the surrounding environment. Thus, 3D mammary tumor spheroids (*i.e.*, mammospheres) enriched with CSLCs have been successfully created by culturing MCF-7 cells with different growth factors and chemicals in order to promote stemness (*i.e.*, self-renewal) and epithelial-to-mesenchymal transition (EMT) as demonstrated by the downregulation of the estrogen receptors (ER) expression whose role appears to be pivotal in maintaining the epithelial differentiation.[122,173] These CD44-expressing mammospheres, which are currently one of the most advanced examples of the 3D systems used for polymer nanocarrier evaluation, allowed assessing the capacity of chitosan-decorated Pluronic127 nanoparticles to efficiently deliver the loaded doxorubicin and to bypass the CSLC drug resistance *in vitro*. Chitosan functionalization resulted in nanoparticles able to selectively target CD44-overexpressing cells in mammospheres (Fig. 10a) while only a minimal targeting was observed in 3D spheroids made of normal human adipose-derived stem cells.[122] The better *in vitro* penetration of such functionalized nanocarriers was also confirmed *in vivo* revealing their highest capacity of inhibition of tumor growth (Fig. 10b and c).

CD44 receptors have been targeted also by chondroitin sulfate A-deoxycholic acid-(3-aminomethylphenyl) boronic acid (CSA-DOCA-AMPB) NPs, which in addition exploited the interaction between boronic acid and sialic acid for efficient delivery of Doxo to human lung adenocarcinoma A549 tumors spheroids.[60] Penetration observed *in vitro* by Confocal Laser Scanning Microscopy (CLSM) was confirmed *in vivo* in A549-tumor bearing mice by three-dimensional near-infrared fluorescence (NIRF) imaging and resulted in significant suppression of tumor development.

2.3.6.4. Monoclonal antibody-targeted nanocarriers. Among the plethora of possible strategies for active targeting, the 2C5 monoclonal antibody (mAb 2C5) has been employed for

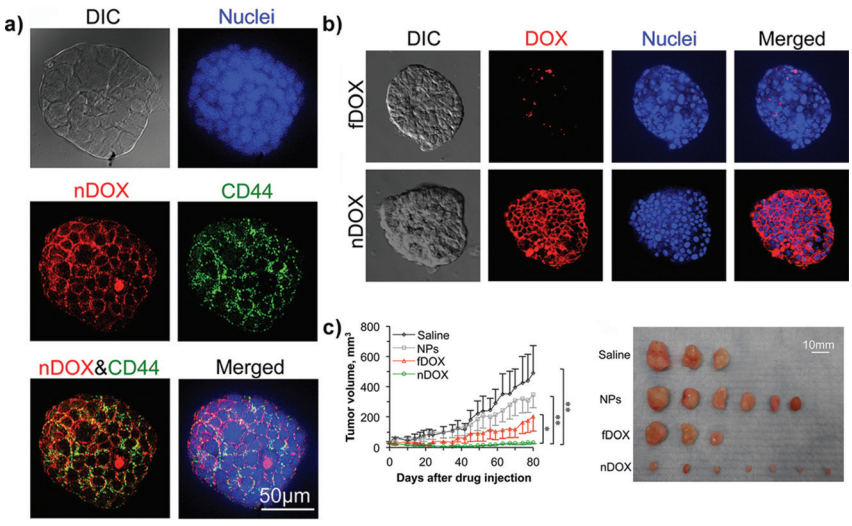

Fig. 10 Structured illumination microscopy (confocal-like) images of the specific binding between chitosan-decorated doxorubicin-loaded nanoparticles (nDOXO) and mammosphere cells: (a) co-localization of nDOXO and CD44 receptors; (b) binding between nDOXO and free Doxo (fDOXO) with mammosphere cells. (c) Tumor volume as a function of time for four different treatments and image of tumors collected on day 80 after the initial drug administration. Reproduced with permission from ref. 122. Copyright 2015 American Chemical Society.

its capacity to target several types of tumor cells thanks to the interaction with the nucleosomes originating from neighboring apoptotically died tumor cells.[174] Nucleosomes are specifically bound to the surface of tumor cells and are always present in the spent media of growing tumor-cell lines as well as in the extracellular fluid of cancer patients.[175] Thus, mAb2C5-functionalized Doxo-loaded polyethylene glycol-phosphatidyl ethanolamine (PEG-PE) micelles have been formulated and evaluated *in vitro* on ovarian cancer MCTS constructed by using NCI-ADR-RES cells.[136] The key role played by this Doxo-resistant MCTS model relied on the Bcl-2 gene overexpression associated with the three dimensional organization of the tumor cells, which closely mimicked the real situation found in patients. Consistent with the beneficial effect of mAb2C5 monoclonal antibody conjugation, uniform Doxo distribution throughout the spheroids was achieved only with the targeted micelles. These same PEG-PE micelles have been also functionalized with the single chain fragment variable (scFv) of the monoclonal antibody against glucose transporter-1 (GLUT-1) whose overexpression in cancer cells relies on their continuous requirement for glucose supply. Accordingly, selective targeting of this transmembrane protein might promote the ligand mediated delivery of anticancer drugs.[66,73] The *in vitro* evaluation on a 2D monolayer of U87MG glioblastoma cells revealed that Doxo and curcumin co-encapsulation in GLUT-1-targeted micelles resulted in a significant enhancement of caspase 3 and 7 activity as compared to un-targeted micelles (mono-drug-loaded and two-drug-loaded).[66] Moreover, GLUT-1 targeting improved the penetration of PEG-PE micelles into 3D glioblastoma spheroids of U87MG cells in which the Doxo and curcumin synergistic effect was confirmed by the highest cytotoxicity (approx. 70% cell death) after 5 days of treatment.[66]

An estrogen receptor alpha (ER-α) mAb has been instead used to functionalize the surface of polyacrylic acid (PAA)-coated ion doped NaYF4:Yb,Er upconversion nanoparticles (UCNPs), which have been investigated as a potential early-stage cancer detecting agent.[83] Such functionalization enabled targeting of MCF7 breast cancer cell spheroids (~500 μm) transplanted in a chick embryo chorioallantoic membrane (CAM) aiming at modelling an early stage (*i.e.*, diameter smaller than 2 mm) breast cancer. This model not only mimicked the cell-to-cell and cell-to-microenvironment interactions but also displayed a novel vascularization around the transplanted spheroid. Being more convenient and easy to handle compared to *in vivo* animal models, this simplified system allowed a direct microscopy study of the UCNPs-mAb's ability to target cancer cells and thus detect tumors *in vivo* at an early-stage. Indeed, following a systemic administration of UCNPs-mAb *via* venule injection under a stereomicroscope, a strong upconversion luminescence was observed in the spheroid mass. It should be noted that only cancer cells were targeted and that no accumulation in the other surrounding tissues of the embryo was observed, thus demonstrating the optimal selective capacity of such modified nanoparticles.

2.3.6.5. Aptamer-targeted nanocarriers. Nucleic acid aptamers (DNA and RNA) capable of recognizing with high specificity the epithelial cell adhesion molecule (EpCAM), a type I membrane protein expressed on the surface of a variety of cancer cells,[176] have been used for surface functionalization of poly(lactide-*co*-glycolide) (PLGA)[75] and alginate-coated chitosan nanoparticles (CHNPs)[74] whose efficiency has been evaluated *in vitro* on 3D MCTS models of breast[75] and colon cancers.[74] Decoration with locked nucleic acid (LNA) aptamers allowed CHNPs to reach colon cancer EpCAM-expressing cells deeply in the core of both 3D MCTS and tumor experimental models in mice.[74] Proof of their being potential efficient drug carriers was provided using CHNPs loaded with the apoptotic agent SR9, a survivin antagonist. Compared to non-functionalized nanoparticles, their efficient targeting and penetration capacity resulted in a 5-fold reduction of spheroid volume *in vitro* (after 72 h exposure) and up to 4 times lower tumor volume in colon cancer xenografts in mice (at d = 70 post tumor induction).[74]

2.3.6.6. Peptide-targeted nanocarriers. Specific recognition of $\alpha_v\beta_3$ integrins has been demonstrated to endow RDG-functionalized nanocarriers with a targeting capacity toward cancer cells facilitating their internalization.[177] Accordingly, the linear or cyclic version of the RGD has been covalently linked to:

(i) micelles made by the assembly of the enzyme-sensitive peptide-linked poly(ethylene glycol) and partially hydrolyzed poly(β-benzyl L-aspartate) (PEG-GPLGVRGDG-P(BLA-*co*-Asp)) co-polymer;[138]

(ii) mesoporous silica nanoparticles (MSNs) coated with poly(ethylene glycol) (PEG), polyethyleneimine (PEI) or chitosan;[84]

(iii) PEG-poly(trimethylene carbonate) (PEG-PTMC) nanoparticles;[63,64]

(iv) poly(amidoamine) (PAMAM) dendrimers.[146,149,150]

The influence of the extent of RGD functionalization was also investigated. For instance, the transfection efficiency of PAMAM-RGD dendrimers displaying various levels of RDG ligands was evaluated in a 3D spheroid model of glioma in comparison with the conventional 2D culture of U87MG cells.[149,150] In 2D cultures no advantage was observed compared to the naked PAMAM, probably as a consequence of the predominant non-specific interaction mediated by the positively charged dendrimers with the cell membrane. However, the evaluation in 3D spheroids highlighted the capacity of PAMAM-RGD to strongly interfere with the $\alpha_v\beta_3$ integrin-mediated interaction of cells with the ECM, which was directly correlated to the number of ligands conjugated to PAMAM. As a consequence of the reduced adhesion, RGD functionalization facilitated the penetration and the uptake of PAMAM dendrimers into the spheroid model although it did not result in a significant gene silencing.[149]

In addition to the capacity of interaction with integrins, conferred by the RGD sequence, the so-called tumor penetrating peptides (TPP)[177,178] display a C-terminal sequence R/KXXR/K known as the C-end rule (CendR).[62,63,80] Together,

these two sequences mediate an active transport through tumor vessels and within the extravascular tumor tissue by interaction first with the $\alpha_v\beta_3$-integrin and then with the neuropilin-1 receptor (NRP).[59,80] Clearly such modification represents a valuable approach for increasing the penetration of nanocarriers in the tumor mass.[56,62,117]

Among the TPP, the iRGD has been physically adsorbed onto boronic acid-rich chitosan-poly(*N*-3-acrylamidophenyl boronic acid) (CS-PAPBA) nanoparticles,[117] or covalently linked to Pluronic F127 coated paclitaxel nanocrystals.[56] CLSM images of spheroids exposed to fluorescently TPP-functionalized nanocarriers revealed an intense signal, which spread from the periphery toward the center of the spheroids, demonstrating their superior capacity of penetration and accumulation leading to an efficient drug delivery confirmed *in vitro* by the reduction of spheroid volume and *in vivo* by the inhibition of tumor progression (Fig. 11).[56,62,89,117]

The use of the simple CendR motif with the RGERPPR sequence has also been proposed to increase the penetrating capacity of poly(ethylene glycol)-polyethylenimine/plasmid DNA complexes resulting in a higher accumulation into a glioma spheroid model (U87MG cells) compared to the non-functionalized counterpart. Nevertheless whether or not the peptide could also be efficient at improving the transfection efficacy in this 3D model still needs to be verified.[80]

Cell penetrating properties are also displayed by the interleukin-13 peptide (IL-13p) capable of specific recognition of the IL13Rα2, a tumor-restricted receptor overexpressed in gliomas. Functionalization of poly(ethylene glycol)-poly(ε-caprolactone) (PEG-PCL) nanoparticles with this peptide (ILNPs) resulted in an enhanced cell-uptake and penetration in U87MG spheroids.[78] A 3-fold higher tumor accumulation was obtained *in vivo* compared to un-functionalized nanoparticles, which resulted in a better docetaxel delivery and a significant reduction of tumor weight compared to the other treatments (saline, free drug and drug-loaded naked NPs).[78] Endowing these NPs with dual targeting properties by functionalization with both IL-13p and RGD peptides further improved their penetration ability in C6 glioma spheroids as well as *in vivo* in orthotopic glioma-bearing mice.[79]

2.4. Use of 3D MCTS to evaluate macromolecules-loaded nanomedicines

Polymer-based nanomedicines have been investigated for the delivery of proteins or DNA/RNA molecules, whose application in clinical settings is strongly limited by (i) inappropriate size and surface charge; (ii) low stability against enzymatic degradation and (iii) low cell membrane permeability.[179,180]

A variety of polymer/siRNA and pDNA polyplexes have been constructed and evaluated in 3D models demonstrating their efficiency as drug carriers. Complexation has been realized for instance with (i) poly(amidoamine) (PAMAM) dendrimers;[92,149] (ii) folate-functionalized-poly(ethylene glycol)-polyamidoamine-polyethylenimine (PME-(PEG-FA)) copolymers[94] (see also section 2.3.6.2); (iii) poly(L-lysine);[118] (iv) PEG-*b*-poly(*N*-substituted asparagine) copolymers(PEG-*b*-P[Asp(DET)]);[131] (v) triblock poly(2-ethyl-2-oxazoline)-poly(L-lactide)-*g*-poly(ethylenimine) (PEOz-PLA-*g*-PEI) polymers;[108,109] (vi) mPEG-PEI (CendR-penetrating-peptide-modified methoxy poly(ethylene glycol)-polyethylenimine) copolymers[80] (see also section 2.3.6.6); (vii) folate-poly(ethylene glycol) (PEG)-Amino Acid Modified Chitosan (CM-PFA)[107] or (viii) poly[(*N*,*N*-dimethylamino) ethyl methacrylate] (PDMAEMA)-derivatized albumin.[93,116]

The pioneering studies of Kataoka and coworkers have highlighted the utility of human hepatocarcinoma multicellular spheroids (HuH-7 cells) for the long-term evaluation of the transfection efficacy achieved using polyplex micelles as gene delivery systems.[118,131] In particular, core–shell type micelles assembled through electrostatic interactions between poly(L-lysine) and lactosylated poly(ethylene glycol)-siRNA conjugate (lac-PEGylated polyplexes)[118] or pDNA and PEG-*block*-poly(*N*-asparagine) copolymers (PEG-*b*-P[Asp(DET)])[131] have been investigated. Only the 3D MCTS spheroids, which can be maintained in culture for several weeks, allowed carrying out an extended analysis of gene expression/suppression under conditions close to those observed *in vivo* in solid tumors.[118] In

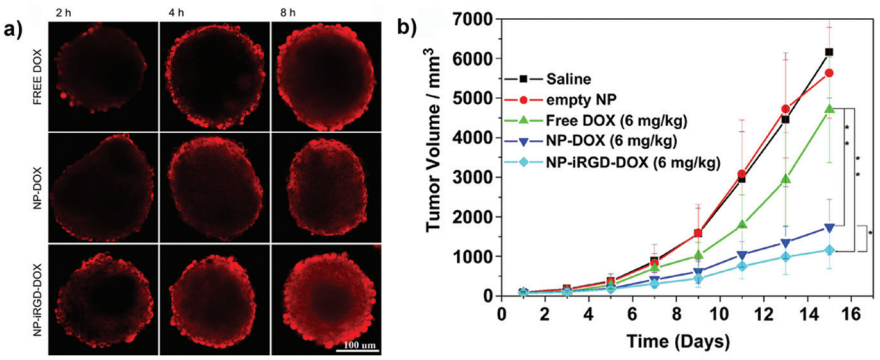

Fig. 11 (a) CLSM images of SH-SY5Y MCTS incubated with free Doxo, Doxo-loaded CS-PAPBA NPs and Doxo-loaded iRGD-CS-PAPBA NPs for 2 h, 4 h and 8 h, respectively. (b) *In vivo* tumor growth curves of H22 tumor-bearing mice that received different treatments. Data are presented as the mean ± SD (n = 10). * represents $P < 0.05$ since the 7th day and ** represents $P < 0.01$ since the 11th day. Reproduced with permission from ref. 117. Copyright 2013 American Chemical Society.

contrast, such time dependent studies could not be performed on 2D monolayer cultures as a consequence of cell–cell contact-induced arrest and viability decrease that prevented the monitoring of a prolonged gene expression.[131] Thus, it was possible to observe that the delivery of the RecQL1 siRNA using the lac-PEGylated polyplexes allowed an efficient suppression of gene expression, which resulted in the inhibition of spheroid growth for up to 21 days.[118] Using the same 3D model it was possible to demonstrate that pDNA-loaded PEGylated polyplexes penetrated in the spheroids and stably induced the expression of the encoded yellow fluorescent protein *Venus* for more than 10 days.[131]

A successful prediction of *in vivo* transfection efficiency was obtained following an evaluation in MDA-MB-231 breast cancer spheroids of heptafluorobutyric acid modified generation 4 (G4) poly(amidoamine) (PAMAM) dendrimers (G4-F735) loaded with a plasmid encoding for the TRAIL (tumor necrosis factor-related apoptosis-inducing ligand) gene.[92] Improved gene delivery and better performance, compared to both naked pTRAIL and conventional transfection reagent poly (ethylene imine) (PEI), were confirmed *in vitro* by the complete degradation of the MDA-MB-231 spheroids after 7 days of treatment (Fig. 12a) and *in vivo* by suppression of tumor growth in a subcutaneous model of luciferase expressing MDA-MB-231 cells (Fig. 12b).[92]

The usefulness of stimuli-responsive approaches was assessed by Gaspar and coworkers.[108,109] Using minicircle DNA (mcDNA), micelleplexes have been constructed by self-assembly of poly(2-ethyl-2-oxazoline)-poly(L-lactide)-*g*-poly (ethylenimine) (PEOz-PLA-*g*-PEI) triblock co-polymer or its bioreducible analogue (PEOz-PLA-*g*-PEI-SS), which allowed the formulation of stimuli-responsive micelles thanks to the introduction of redox sensitive bonds.[108] Both systems displayed a good penetration ability and negligible cytotoxicity in 3D MCTS models of melanoma (B16F12 cells), cervix carcinoma (HeLa cells)[108] and breast cancer (MCF-7 cells).[109] Nevertheless, confocal images of 3D HeLa and B16F10 spheroid sections revealed that bioreducible micelleplexes enhanced GFP gene expression thanks to a higher mcDNA release following rapid intracellular reduction of the disulfide linkages.[108]

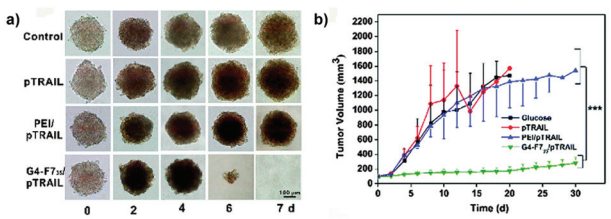

Fig. 12 (a) Optical images of MDA-MB-231 MCTS treated with a fresh medium (control), naked pTRAIL (pTRAIL), poly(ethylene imine)/pTRAIL complex (PEI/pTRAIL) and G4-F735/pTRAIL complex (G4-F735/pTRAIL) at different time points. (b) Time-elapsed evolution of tumor sizes *in vivo*. Reproduced with permission from ref. 92. Copyright 2016 Royal Society of Chemistry.

2.5. Miscellaneous nanocarriers evaluated on 3D MCTS

Surface modification of inorganic nanoparticles with various polymers might make possible their use as theranostic systems for efficient delivery of therapeutic molecules and precise monitoring of the response.[81] In this view, coating of iron oxide nanoparticles (IONPs, MRI contrast agent) with poly(4-O-acryloyl benzaldehyde)-poly(oligoethylene glycol acrylate) P(HBA)-*b*-P(OEGA) block copolymers allowed their stabilization as well as the covalent conjugation of doxorubicin *via* a pH-sensitive bond, which assured drug release in an acidic environment (pH 5.5).[81] 3D optical sectioning by multi-photon microscopy of multicellular spheroids made of lung (H129) or breast (MCF7) cancer cells clearly showed the fluorescence of Doxo-loaded IONP@P(HBA)-*b*-P(OEGA) nanoparticles uniformly spread across the spheroid tissue highlighting a complete penetration after 17 h of incubation; in contrast, free Doxo accumulated in the periphery reaching a maximal depth of 40 μm only (Fig. 13).[81]

Real time monitoring of tumor response to treatment is the goal pursued by Oishi and coworkers with the formulation of a PEGylated nanogel containing gold nanoparticles in the cross-linked poly[2-(*N*,*N*-diethylamino)ethyl methacrylate] (PEAMA) core in which fluorescein isothiocyanate (FITC) was linked to the PEG chains using the Asp-Glu-Val-Asp (DEVD) peptide sequence as a caspase-3-cleavable linker.[156] Based on the Fluorescence Resonance Energy Transfer (FRET) between gold nanoparticles (*i.e.*, fluorescent quencher) and FITC, such a system behaved as a caspase-3-responsive apoptosis sensor for precise *in vitro* monitoring of the activity of apoptosis-inducing agents. The proof of concept has been provided using human hepatocyte MCTS (HuH-7 cells), which have been incubated with nanogels for 24 h prior to exposure to the apoptotic drug

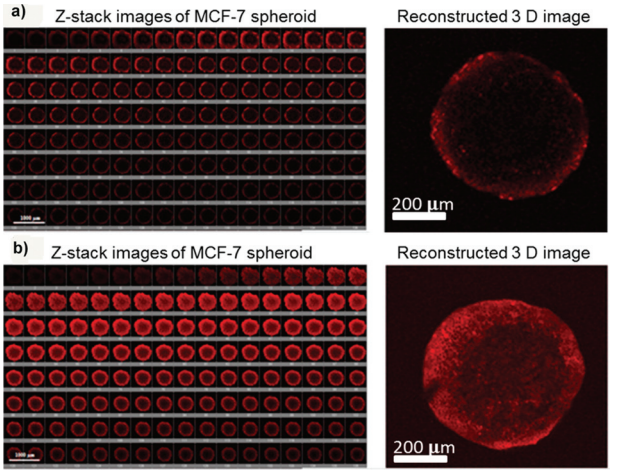

Fig. 13 3D images of MCF-7 spheroids after incubation with (a) free Doxo and (b) Doxo-loaded IONP@P(HBA)-*b*-P(OEGA) for 17 h. The representative confocal images (left) were taken every 5 μm section from the top to bottom in the middle of an intact spheroid, whereas the 3D image (right) was reconstructed using Imaris software. Reproduced with permission from ref. 81. Copyright 2013 American Chemical Society.

staurosporine for 4 h. Intracellular caspase activation triggered FITC release from the nanogels and the dequenching of the fluorescent signal, which allowed assessing the early stage activation of the induced apoptotic pathway.

The application of nanodiamonds (ND) as drug delivery systems is currently strongly limited by their tendency to agglomerate and precipitate in solution. Thus whether surface modification with polymers might offer a beneficial effect has been explored by the grafting of poly(1-O-methacryloyl-2,3:4,5-di-O-isopropylidene-β-D-fructopyranose) (poly-(1-O-MAipFru)$_{62}$) onto the surface of amine-functionalized ND. Such an approach should improve their stability and allow a successful loading of doxorubicin.[157] When evaluated in 2D monolayer cultures of MCF-7 and MDA-MB-231 breast cancer cells, a clear superiority of the free drug over the NDs was observed. However, in 3D breast cancer MCTS (MCF-7 cells) long term exposure (8 days) to the Doxo-loaded poly(1-O-MAFru)$_{62}$-ND resulted in higher cytotoxicity compared to the free drug, which can be justified by the deeper penetration of NDs in spheroids and the sustained release of the drug. In contrast, the free Doxo was rapidly internalized by the proliferating cells of the outer layers of the spheroids and the consequent cell death hindered further penetration.[157]

3. Combining 3D MCTS and polymer scaffolds

3D tumor models made of multicellular spheroids surrounded by a polymer scaffold have also been proposed as an alternative to simple spheroids suspended in cell culture medium. In these systems the scaffold building materials create a matrix around the spheroid capable of mimicking *in vitro* the microenvironment surrounding the tumors *in vivo.* Accordingly, this additional barrier may offer the possibility of discerning better the capacity of various nanocarriers to diffuse and to reach the cancer cells.

One of the simplest strategies consisted in embedding preformed spheroids into a collagen gel. Such a system enabled for instance highlighting the better efficacy of paclitaxel loaded into pH sensitive NPs (*i.e.*, espansile NPs)[181] compared to the free drug, while this difference did not appear in 2D cultures. Indeed, the latter did not display any difference in the cell response independently of the drug administration method (free drug solution *vs.* drug-loaded nanocarrier).[65] In contrast, in 3D cultures, drug-loaded nanoparticles induced a more important slowing of the spheroid growth, which mirrored the inhibition of tumor progression obtained *in vivo* in tumor-bearing mice.[181]

In another 3D spheroid design a single cell suspension has been mixed with collagen before gelification and cells aggregated over time inside the matrix in the form of spheres. Again, while no differences were observed in 2D between the free drug (5-fluorouracil) and the drug-loaded micelles, in contrast, thanks to the presence of the collagen matrix which mimicked the tumor ECM, the 3D model enabled revealing the limited diffusive capacity of micelles (152 nm) compared to the small molecules that led to a lower cytotoxicity.[182] The same strategy has been applied by mixing prostate cancer cells with hyaluronic acid,[183] one of the components of the stroma associated with this tumor *in vivo*, which not only provided structural support but also strongly influenced tumor cell morphology, gene expression and tumorigenic potential.[184] For instance, cells cultured in this 3D scaffold displayed higher expression of multidrug resistance proteins, probably as a result of the limited availability of oxygen and nutrients. Accordingly, while in the 2D cultures the free drug (doxorubicin) easily reached the nucleus and exerted its therapeutic activity, in 3D the sensitivity to the free doxorubicin was reduced (5 μM *vs.* 15 μM, respectively). Contrariwise, independently of the culture conditions the response to Doxo-loaded PEG-PCL NPs was not modified and analogous IC_{50} values were measured (11 μM *vs.* 12.3 μM, respectively) probably thanks to the capacity of these NPs (54 nm diameter) to overcome the MDR while the free drug undergoes a rapid efflux, which reduced its efficacy.[183]

4. Combining 3D MCTS and microfluidic devices

Undoubtedly, compared to simplistic 2D cultures the above-described 3D systems enabled a more predictive *in vitro* screening of nanoscale systems for drug delivery. Nevertheless, due to the lack of fluid dynamics these setups mimic only a static condition. To face this issue, microfluidic devices, which combine 3D culture and controlled flow conditions, have been recently developed with the aim: (i) to assess how physicochemical parameters influence the transport through tumor biological barriers under dynamic conditions and (ii) to provide information on the optimal design required to achieve a successful tumor accumulation.[185,186]

For instance, a tumor-on-a-chip device allowed the passage from a static spheroid culture to a dynamic situation by placing a spheroid in the channel of a two layer poly(diméthylsiloxane) (PDMS) chip (Fig. 14a).[185] By tuning the flow rate in the device, fluid velocities and shear stresses similar to the blood flow in capillary vessels (75–675 μm s^{-1}) or the interstitial flow inside a tumor (0.1–3 μm s^{-1}) could be reproduced in a controllable manner. Exposure of spheroids to PEGylated nanoparticles of different sizes under stationary flow revealed interstitial accumulation only of the smaller NPs (40 nm) while the larger ones (110 nm), bigger than the ECM pores, were excluded (Fig. 14b and c). However, accumulation was only transient and nanoparticles flowed out after flushing, confirming that surface modification with PEG chains hindered the establishment of specific interactions with cells and ECM components. In contrast, no efflux was observed following NP functionalization with transferrin and 40 nm nanoparticles showed up to 15-fold increase of tumor accumulation compared to non-functionalized NPs. It was also observed that an increase of the flow rate resulted in accumulation in the

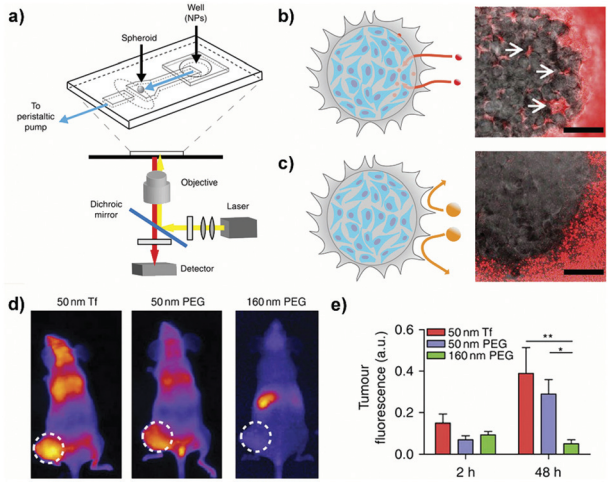

Fig. 14 (a) Schematic of the PDMS microfluidic device on a microscope stage. (b) Schematic (left) and image (right) of 40 nm fluorescent PEG-NPs administered for 1 h at 50 μL h^{-1} entering the spheroid and accumulating in the interstitial spaces (arrows). Scale bar: 100 μm. (c) Schematic (left) and image (right) of 110 nm fluorescent PEG-NPs administered for 1 h at 50 μL h^{-1} being excluded from the spheroid. Scale bar: 100 μm. (d) Representative images of tumor fluorescence from mice injected with NPs in the tail vein at 48 h post-injection. (e) Quantification of animal fluorescence at 2 and 48 h using whole animal images. Reproduced with permission from ref. 185. Copyright 2013 Nature Publishing Group.

external spheroid layer, forming a tissue–fluid interface reservoir but that did not affect the depth of NP penetration. When the NPs were then tested *in vivo* in a tumor bearing mice, the same size discriminating effect was recorded, with a better accumulation of small NPs (50 nm) compared to the larger ones (160 nm). However, functionalization did not lead to any significant advantage and both targeted and non-targeted 50 nm NPs displayed similar tumor accumulation levels (Fig. 14d and e). Such contradiction with the results obtained *in vitro* clearly highlighted a limit of the 3D models, which cannot fully reproduce the complexity of living organisms and the behavior of NPs after intravenous administration. Thus, although it is evident that 3D models would allow a more relevant preclinical screening of nanomedicines compared to 2D cultures, at

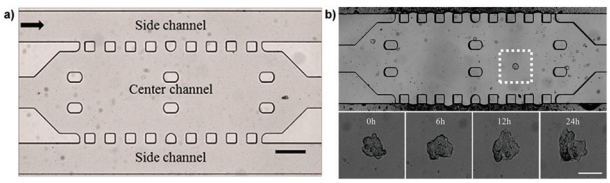

Fig. 15 (a) Bright field image of the microfluidic channel. The black arrow shows the direction of medium flow. Scale bar: 300 μm. (b) Bright-field image of the MCTS in the microfluidic channel. (top) The MCTS in Matrigel prior to Doxo-HCl treatment. (bottom) Real-time, enlarged views of the MCTS during 24 h of treatment with Doxo-HCl. Scale bar: 50 μm. Reproduced with permission from ref. 187. Copyright 2013 American Chemical Society.

present they cannot completely replace the *in vivo* experimentation.

Another proposed approach consisted in the loading of Matrigel-embedded preformed spheroids in the central channel of a microfluidic device, while continuous medium addition in the lateral channels recreated some blood flow conditions. This allowed to assess under dynamic conditions treatment responses to doxorubicin in free form and loaded into micelles (Fig. 15).[187]

5. Conclusion and perspectives

Through many literature examples this review has unambiguously highlighted that simple 2D monolayers cultures do not allow a complete understanding of the therapeutic potential of polymer nanomedicines while the application of 3D tumor models in preclinical evaluation would provide more accurate results, predictive of the *in vivo* pharmacological efficacy. The key features of the MCTS (*e.g.*, presence of ECM, diffusive gradients, complex cell signaling, drug resistance and metabolic adaptation) undoubtedly enable evaluating the nanomedicines under conditions closer to the clinical reality. But it cannot be ignored that the majority of tumor spheroids used in the literature are made of cancer cells alone and therefore they just represent a rather simplified model of real tumorigenesis. Due to the complexity of the tumor tissues and the cross-talk between cancer cells and their microenvironment, advanced models including several cell types (*e.g.*, endothelial cells, immune cells, fibroblasts *etc.*) and components of the ECM are urgently required. Thus, 3D co-cultures[47,48,188] and microfluidic devices[111–113,185,186,189] have been developed but further improvements are still needed in order to allow wider application in preclinical investigation. In this context, the accurate characterization (*e.g.*, cell number, long term viability of each cell component, type of ECM protein, *etc.*) of any developed system is mandatory for allowing a reliable interpretation of the obtained results. It is indeed well acknowledged that the spheroid size[43,46] as well as the presence of stroma components[47,48,188] strongly affect the response to treatment according to the possible development of penetration barriers,[46–48,188] chemical gradients and/or necrosis.[43]

The availability of microscopy techniques suitable for high resolution imaging of 3D cell cultures is another challenge. Indeed, although widely used, CLSM does not allow the *in toto* study of large 3D samples and the obtained results refer only to penetration into the spheroids at the depth of a maximum of 100–150 μm. A significant improvement in 3D imaging should result from Two-Photon (TPM) and Multi-Photon Microscopy (MPM) studies but the low spatial resolution along the optical axis and the incompatibility of certain fluorophores with the multi-photon excitation still restrict the applicability of these methods.[140,190] In this challenging panorama, LSFM approaches (*e.g.*, Selective Plane Illumination Microscopy (SPIM)) are emerging as techniques of choice in life sciences for the imaging of complex and highly scattering

samples.[142–145] Offering the possibility of visualizing the spheroids in their entirety with a sub-cellular resolution[191,192] the SPIM technique clearly enables achieving a superior degree of information in the screening of nanomedicines' pharmacological efficiency.[47] The penetration ability of nanomedicines can be assessed over the whole 3D MCTS mass and a dynamic study of the anticancer response is also possible with the time lapse imaging of living spheroids. Unfortunately, such advanced techniques require highly specialized technologies whose availability still remains limited.

It is evident that labor-intensive handling, time-consuming procedures, instrumental limitations and costs still hinder the routine use of advanced 3D models in drug discovery programmes. It is noteworthy that, to the best of our knowledge, no promising nanomedicine currently in clinical trials has been tested in 3D MCTS during *in vitro* preclinical studies. Nevertheless, advances in the near future are expected to rapidly support their widespread use, thus making the *in vitro* drug screenings more predictive and able to sieve out underperforming compounds in the early preclinical stage.

Acknowledgements

The authors acknowledge financial support from the European Union's Horizon 2020 research and innovation programme under Marie Skłodowska Curie grant agreement no. 642028, the CNRS and the French Ministry of Research.

Notes and references

1 D. Peer, J. M. Karp, S. Hong, O. C. Farokhzad, R. Margalit and R. Langer, *Nat. Nanotechnol.*, 2007, **2**, 751–760.
2 M. W. Tibbitt, J. E. Dahlman and R. Langer, *J. Am. Chem. Soc.*, 2016, **138**, 704–717.
3 P. Couvreur and C. Vauthier, *Pharm. Res.*, 2006, **23**, 1417–1450.
4 J. Nicolas, S. Mura, D. Brambilla, N. Mackiewicz and P. Couvreur, *Chem. Soc. Rev.*, 2013, **42**, 1147–1235.
5 S. Mura, J. Nicolas and P. Couvreur, *Nat. Mater.*, 2013, **12**, 991–1003.
6 C. A. Schütz, L. Juillerat-Jeanneret, H. Mueller, I. Lynch and M. Riediker, *Nanomedicine*, 2013, **8**, 449–467.
7 A. K. Lytton-Jean, K. J. Kauffman, J. C. Kaczmarek and R. Langer, *Cancer Treat. Res.*, 2015, **166**, 293–322.
8 A. C. Anselmo and S. Mitragotri, *Bioeng. Transl. Med.*, 2016, **1**, 10–29.
9 M. E. Davis, Z. G. Chen and D. M. Shin, *Nat. Rev. Drug Discovery*, 2008, **7**, 771–782.
10 N. V. Tsarevsky and K. Matyjaszewski, *Chem. Rev.*, 2007, **107**, 2270–2299.
11 O. Dechy-Cabaret, B. Martin-Vaca and D. Bourissou, *Chem. Rev.*, 2004, **104**, 6147–6176.
12 C. Boyer, V. Bulmus, T. P. Davis, V. Ladmiral, J. Liu and S. Perrier, *Chem. Rev.*, 2009, **109**, 5402–5436.
13 J. Nicolas, Y. Guillaneuf, C. Lefay, D. Bertin, D. Gigmes and B. Charleux, *Prog. Polym. Sci.*, 2013, **38**, 63–235.
14 S. Wilhelm, A. J. Tavares, Q. Dai, S. Ohta, J. Audet, H. F. Dvorak and W. C. W. Chan, *Nat. Rev. Mater.*, 2016, **1**, 16014.
15 E. Blanco, H. Shen and M. Ferrari, *Nat. Biotechnol.*, 2015, **33**, 941–951.
16 P. Lu, V. M. Weaver and Z. Werb, *J. Cell Biol.*, 2012, **196**, 395–406.
17 K. M. Bussard, L. Mutkus, K. Stumpf, C. Gomez-Manzano and F. C. Marini, *Breast Cancer Res.*, 2016, **18**, 84.
18 M. W. Pickup, J. K. Mouw and V. M. Weaver, *EMBO Rep.*, 2014, **15**, 1243–1253.
19 A. Birgersdotter, R. Sandberg and I. Ernberg, *Semin. Cancer Biol.*, 2005, **15**, 405–412.
20 E. Cukierman, R. Pankov, D. R. Stevens and K. M. Yamada, *Science*, 2001, **294**, 1708–1712.
21 D. R. Albrecht, G. H. Underhill, T. B. Wassermann, R. L. Sah and S. N. Bhatia, *Nat. Methods*, 2006, **3**, 369–375.
22 M. W. Tibbitt and K. S. Anseth, *Biotechnol. Bioeng.*, 2009, **103**, 655–663.
23 C. H. Heldin, K. Rubin, K. Pietras and A. Ostman, *Nat. Rev. Cancer*, 2004, **4**, 806–813.
24 L. G. Griffith and M. A. Swartz, *Nat. Rev. Mol. Cell Biol.*, 2006, **7**, 211–224.
25 M. C. Cox, L. M. Reese, L. R. Bickford and S. S. Verbridge, *ACS Biomater. Sci. Eng.*, 2015, **1**, 877–894.
26 C. Fischbach, R. Chen, T. Matsumoto, T. Schmelzle, J. S. Brugge, P. J. Polverini and D. J. Mooney, *Nat. Methods*, 2007, **4**, 855–860.
27 C. R. Thoma, M. Zimmermann, I. Agarkova, J. M. Kelm and W. Krek, *Adv. Drug Delivery Rev.*, 2014, **69–70**, 29–41.
28 L. B. Weiswald, D. Bellet and V. Dangles-Marie, *Neoplasia*, 2015, **17**, 1–15.
29 X. Xu, M. C. Farach-Carson and X. Jia, *Biotechnol. Adv.*, 2014, **32**, 1256–1268.
30 A. Nyga, U. Cheema and M. Loizidou, *J. Cell Commun. Signal.*, 2011, **5**, 239–248.
31 W. Asghar, R. El Assal, H. Shafiee, S. Pitteri, R. Paulmurugan and U. Demirci, *Mater. Today*, 2015, **18**, 539–553.
32 K. A. Fitzgerald, M. Malhotra, C. M. Curtin, F. J. O'Brien and C. M. O'Driscoll, *J. Controlled Release*, 2015, **215**, 39–54.
33 J. Tannenbaum and B. T. Bennett, *J. Am. Assoc. Lab. Anim. Sci.*, 2015, **54**, 120–132.
34 A. Abbott, *Nature*, 2003, **424**, 870–872.
35 R. M. Sutherland, J. A. Mccredie and W. R. Inch, *J. Natl. Cancer Inst.*, 1971, **46**, 113–120.
36 R. Sutherland, J. Carlsson, R. Durand and J. Yuhas, *Cancer Res.*, 1981, **41**, 2980–2984.
37 D. V. LaBarbera, B. G. Reid and B. H. Yoo, *Expert Opin. Drug Discovery*, 2012, **7**, 819–830.
38 S. Breslin and L. O'Driscoll, *Drug Discovery Today*, 2013, **18**, 240–249.
39 J. C. Lovitt, B. T. Shelper and M. V. Avery, *Biology*, 2014, **3**, 345–367.

40 E. C. Costa, A. F. Moreira, D. de Melo-Diogo, V. M. Gaspar, M. P. Carvalho and I. J. Correia, *Biotechnol. Adv.*, 2016, **34**, 1427–1441.
41 E. Fennema, N. Rivron, J. Rouwkema, C. van Blitterswijk and J. de Boer, *Trends Biotechnol.*, 2013, **31**, 108–115.
42 G. Hamilton, *Cancer Lett.*, 1998, **131**, 29–34.
43 F. Hirschhaeuser, H. Menne, C. Dittfeld, J. West, W. Mueller-Klieser and L. A. Kunz-Schughart, *J. Biotechnol.*, 2010, **148**, 3–15.
44 R.-Z. Lin and H.-Y. Chang, *Biotechnol. J.*, 2008, **3**, 1172–1184.
45 G. Mehta, A. Y. Hsiao, M. Ingram, G. D. Luker and S. Takayama, *J. Controlled Release*, 2012, **164**, 192–204.
46 A. Kang, H. I. Seo, B. G. Chung and S.-H. Lee, *Nanomedicine*, 2015, **11**, 1153–1161.
47 P. Sethi, A. Jyoti, E. P. Swindell, R. Chan, U. W. Langner, J. M. Feddock, R. Nagarajan, T. V. O'Halloran and M. Upreti, *Nanomedicine*, 2015, **11**, 2013–2023.
48 D. L. Priwitaningrum, J.-B. G. Blondé, A. Sridhar, J. van Baarlen, W. E. Hennink, G. Storm, S. Le Gac and J. Prakash, *J. Controlled Release*, 2016, **244**(Part B), 257–268.
49 J. Friedrich, R. Ebner and L. A. Kunz-Schughart, *Int. J. Radiat. Biol.*, 2007, **83**, 849–871.
50 P. Benien and A. Swami, *Future Oncol.*, 2014, **10**, 1311–1327.
51 N. R. Patel, B. Aryasomayajula, A. H. Abouzeid and V. P. Torchilin, *Ther. Delivery*, 2015, **6**, 509–520.
52 Q. Yang, Y. Yang, L. Li, W. Sun, X. Zhu and Y. Huang, *ACS Appl. Mater. Interfaces*, 2015, **7**, 6661–6673.
53 X. Wei, T. H. Senanayake, G. Warren and S. V. Vinogradov, *Bioconjugate Chem.*, 2013, **24**, 658–668.
54 H. Lei, S. C. Hofferberth, R. Liu, A. Colby, K. M. Tevis, P. Catalano, M. W. Grinstaff and Y. L. Colson, *J. Thorac. Cardiovasc. Surg.*, 2015, **149**, 1417–1424.
55 X. Cheng, X. Wang, Z. Cao, W. Yao, J. Wang and R. Tang, *Mater. Sci. Eng., C*, 2017, **71**, 298–307.
56 D. Ni, H. Ding, S. Liu, H. Yue, Y. Bao, Z. Wang, Z. Su, W. Wei and G. Ma, *Small*, 2015, **11**, 2518–2526.
57 Z. Cao, X. Wang, X. Cheng, J. Wang and R. Tang, *Int. J. Polym. Mater. Polym. Biomater.*, 2017, **66**, 495–506.
58 G. Yan, Q. Zha, J. Wang, X. Wang, X. Cheng, W. Yao and R. Tang, *Polymer*, 2017, **111**, 192–203.
59 S. Ma, J. Zhou, Y. Zhang, Y. He, Q. Jiang, D. Yue, X. Xu and Z. Gu, *ACS Appl. Mater. Interfaces*, 2016, **8**, 28468–28479.
60 J.-Y. Lee, S.-J. Chung, H.-J. Cho and D.-D. Kim, *Adv. Funct. Mater.*, 2015, **25**, 3705–3717.
61 Y. Li, H. He, X. Jia, W.-L. Lu, J. Lou and Y. Wei, *Biomaterials*, 2012, **33**, 3899–3908.
62 Q. Hu, X. Gao, G. Gu, T. Kang, Y. Tu, Z. Liu, Q. Song, L. Yao, Z. Pang, X. Jiang, H. Chen and J. Chen, *Biomaterials*, 2013, **34**, 5640–5650.
63 X. Jiang, H. Xin, J. Gu, X. Xu, W. Xia, S. Chen, Y. Xie, L. Chen, Y. Chen, X. Sha and X. Fang, *Biomaterials*, 2013, **34**, 1739–1746.
64 X. Jiang, X. Sha, H. Xin, X. Xu, J. Gu, W. Xia, S. Chen, Y. Xie, L. Chen, Y. Chen and X. Fang, *Biomaterials*, 2013, **34**, 2969–2979.
65 K. M. Charoen, B. Fallica, Y. L. Colson, M. H. Zaman and M. W. Grinstaff, *Biomaterials*, 2014, **35**, 2264–2271.
66 C. Sarisozen, S. Dhokai, E. G. Tsikudo, E. Luther, I. M. Rachman and V. P. Torchilin, *Eur. J. Pharm. Biopharm.*, 2016, **108**, 54–67.
67 C. Sarisozen, A. H. Abouzeid and V. P. Torchilin, *Eur. J. Pharm. Biopharm.*, 2014, **88**, 539–550.
68 W. Zou, C. Sarisozen and V. P. Torchilin, *J. Drug Targeting*, 2016, **25**, 225–234.
69 X. Cao, X. Zhou, Y. Wang, T. Gong, Z.-R. Zhang, R. Liu and Y. Fu, *J. Mater. Chem. B*, 2016, **4**, 3216–3224.
70 H. L. Ma, Q. Jiang, S. Han, Y. Wu, T. J. Cui, D. Wang, Y. Gan, G. Zou and X. J. Liang, *Mol. Imaging*, 2012, **11**, 487–498.
71 H. E. Colley, V. Hearnden, M. Avila-Olias, D. Cecchin, I. Canton, J. Madsen, S. MacNeil, N. Warren, K. Hu, J. A. McKeating, S. P. Armes, C. Murdoch, M. H. Thornhill and G. Battaglia, *Mol. Pharmaceutics*, 2014, **11**, 1176–1188.
72 J. Bugno, H.-J. Hsu, R. M. Pearson, H. Noh and S. Hong, *Mol. Pharmaceutics*, 2016, **13**, 2155–2163.
73 X. Jiang, H. Xin, J. Gu, F. Du, C. Feng, Y. Xie and X. Fang, *J. Pharm. Sci.*, 2014, **103**, 1487–1496.
74 K. Roy, R. K. Kanwar, C. H. A. Cheung, C. L. Fleming, R. N. Veedu, S. Krishnakumar and J. R. Kanwar, *RSC Adv.*, 2015, **5**, 29008–29016.
75 M. Das, W. Duan and S. K. Sahoo, *Nanomedicine*, 2015, **11**, 379–389.
76 G. L. Hu, Y. Wang, Q. He and H. L. Gao, *RSC Adv.*, 2015, **5**, 85933–85937.
77 S. Sharma, J. Singh, A. Verma, B. V. Teja, R. P. Shukla, S. K. Singh, V. Sharma, R. Konwar and P. R. Mishra, *RSC Adv.*, 2016, **6**, 73083–73095.
78 H. Gao, Z. Yang, S. Zhang, S. Cao, Z. Pang, X. Yang and X. Jiang, *J. Controlled Release*, 2013, **172**, 921–928.
79 H. Gao, Y. Xiong, S. Zhang, Z. Yang, S. Cao and X. Jiang, *Mol. Pharmaceutics*, 2014, **11**, 1042–1052.
80 J. Wang, Y. Lei, C. Xie, W. Lu, Z. Yan, J. Gao, Z. Xie, X. Zhang and M. Liu, *Int. J. Pharm.*, 2013, **458**, 48–56.
81 J. S. Basuki, H. T. T. Duong, A. Macmillan, R. B. Erlich, L. Esser, M. C. Akerfeldt, R. M. Whan, M. Kavallaris, C. Boyer and T. P. Davis, *ACS Nano*, 2013, **7**, 10175–10189.
82 S. Jin, X. Ma, H. Ma, K. Zheng, J. Liu, S. Hou, J. Meng, P. C. Wang, X. Wu and X.-J. Liang, *Nanoscale*, 2013, **5**, 143–146.
83 K. Liu, J. A. Holz, Y. Ding, X. Liu, Y. Zhang, L. Tu, X. Kong, B. Priem, A. Nadort, S. A. Lambrechts, M. C. Aalders, W. J. Buma, Y. Liu and H. Zhang, *Nanoscale*, 2015, **7**, 1596–1600.
84 Y. You, H. Hu, L. He and T. Chen, *Chem. – Asian J.*, 2015, **10**, 2744–2754.
85 R. Agarwal, P. Jurney, M. Raythatha, V. Singh, S. V. Sreenivasan, L. Shi and K. Roy, *Adv. Healthcare Mater.*, 2015, **4**, 2269–2280.

86 A. Ivascu and M. Kubbies, *J. Biomol. Screening*, 2006, **11**, 922–932.
87 J. Friedrich, C. Seidel, R. Ebner and L. A. Kunz-Schughart, *Nat. Protoc.*, 2009, **4**, 309–324.
88 M. Cui, D. J. Naczynski, M. Zevon, C. K. Griffith, L. Sheihet, I. Poventud-Fuentes, S. Chen, C. M. Roth and P. V. Moghe, *Adv. Healthcare Mater.*, 2013, **2**, 1236–1245.
89 D.-S. Liang, H.-T. Su, Y.-J. Liu, A.-T. Wang and X.-R. Qi, *Biomaterials*, 2015, **71**, 11–23.
90 H. X. Lu, R. H. Utama, U. Kitiyotsawat, K. Babiuch, Y. Jiang and M. H. Stenzel, *Biomater. Sci.*, 2015, **3**, 1085–1095.
91 Y. Y. Jiang, H. X. Lu, A. Dag, G. Hart-Smith and M. H. Stenzel, *J. Mater. Chem.*, 2016, **4**, 2017–2027.
92 Y. Wang, M. Wang, H. Chen, H. Liu, Q. Zhang and Y. Cheng, *J. Mater. Chem. B*, 2016, **4**, 1354–1360.
93 Y. Jiang, C. K. Wong and M. H. Stenzel, *Macromol. Biosci.*, 2015, **15**, 965–978.
94 D. Cao, S. Tian, H. Huang, J. Chen and S. Pan, *Mol. Pharmaceutics*, 2015, **12**, 240–252.
95 A. W. Du, H. Lu and M. Stenzel, *Mol. Pharmaceutics*, 2016, **13**, 3648–3656.
96 T. H. Kim, C. W. Mount, W. R. Gombotz and S. H. Pun, *Biomaterials*, 2010, **31**, 7386–7397.
97 T. T. Goodman, P. L. Olive and S. H. Pun, *Int. J. Nanomed.*, 2007, **2**, 265–274.
98 T. T. Goodman, J. Chen, K. Matveev and S. H. Pun, *Biotechnol. Bioeng.*, 2008, **101**, 388–399.
99 S. S. Verbridge, A. Chakrabarti, P. DelNero, B. Kwee, J. D. Varner, A. D. Stroock and C. Fischbach, *J. Biomed. Mater. Res., Part A*, 2013, **101**, 2948–2956.
100 T. Okuyama, H. Yamazoe, N. Mochizuki, A. Khademhosseini, H. Suzuki and J. Fukuda, *J. Biosci. Bioeng.*, 2010, **110**, 572–576.
101 H. Hardelauf, J.-P. Frimat, J. D. Stewart, W. Schormann, Y.-Y. Chiang, P. Lampen, J. Franzke, J. G. Hengstler, C. Cadenas, L. A. Kunz-Schughart and J. West, *Lab Chip*, 2011, **11**, 419–428.
102 Y. Morimoto, A. Y. Hsiao and S. Takeuchi, *Adv. Drug Delivery Rev.*, 2015, **95**, 29–39.
103 M. Cordey, M. Limacher, S. Kobel, V. Taylor and M. P. Lutolf, *Stem Cells*, 2008, **26**, 2586–2594.
104 J. Fukuda, A. Khademhosseini, Y. Yeo, X. Yang, J. Yeh, G. Eng, J. Blumling, C.-F. Wang, D. S. Kohane and R. Langer, *Biomaterials*, 2006, **27**, 5259–5267.
105 T. Liu, I. Kempson, M. de Jonge, D. L. Howard and B. Thierry, *Nanoscale*, 2014, **6**, 9774–9782.
106 S. Ohta, S. Hiramoto, Y. Amano, M. Sato, Y. Suzuki, M. Shinohara, S. Emoto, H. Yamaguchi, H. Ishigami, Y. Sakai, J. Kitayama and T. Ito, *Bioconjugate Chem.*, 2016, **27**, 504–508.
107 V. M. Gaspar, E. C. Costa, J. A. Queiroz, C. Pichon, F. Sousa and I. J. Correia, *Pharm. Res.*, 2015, **32**, 562–577.
108 V. M. Gaspar, P. Baril, E. C. Costa, D. de Melo-Diogo, F. Foucher, J. A. Queiroz, F. Sousa, C. Pichon and I. J. Correia, *J. Controlled Release*, 2015, **213**, 175–191.
109 V. M. Gaspar, C. Gonçalves, D. de Melo-Diogo, E. C. Costa, J. A. Queiroz, C. Pichon, F. Sousa and I. J. Correia, *J. Controlled Release*, 2014, **189**, 90–104.
110 T. Anajafi, M. D. Scott, S. You, X. Yang, Y. Choi, S. Y. Qian and S. Mallik, *Bioconjugate Chem.*, 2016, **27**, 762–771.
111 S. I. Montanez-Sauri, D. J. Beebe and K. E. Sung, *Cell. Mol. Life Sci.*, 2015, **72**, 237–249.
112 R. Sudo, S. Chung, I. K. Zervantonakis, V. Vickerman, Y. Toshimitsu, L. G. Griffith and R. D. Kamm, *FASEB J.*, 2009, **23**, 2155–2164.
113 K. E. Sung, N. Yang, C. Pehlke, P. J. Keely, K. W. Eliceiri, A. Friedl and D. J. Beebe, *Integr. Biol.*, 2011, **3**, 439–450.
114 S. Ghosh, S. Mohapatra, A. Thomas, D. Bhunia, A. Saha, G. Das, B. Jana and S. Ghosh, *ACS Appl. Mater. Interfaces*, 2016, **8**, 30824–30832.
115 W. L. Lee, W. M. Guo, V. H. B. Ho, A. Saha, H. C. Chong, N. S. Tan, E. Y. Tan and S. C. J. Loo, *Acta Biomater.*, 2015, **27**, 53–65.
116 Y. Jiang, H. Lu, F. Chen, M. Callari, M. Pourgholami, D. L. Morris and M. H. Stenzel, *Biomacromolecules*, 2016, **17**, 808–817.
117 X. Wang, X. Zhen, J. Wang, J. Zhang, W. Wu and X. Jiang, *Biomaterials*, 2013, **34**, 4667–4679.
118 M. Oishi, Y. Nagasaki, N. Nishiyama, K. Itaka, M. Takagi, A. Shimamoto, Y. Furuichi and K. Kataoka, *ChemMedChem*, 2007, **2**, 1290–1297.
119 J. Li, Y. Han, Q. Chen, H. Shi, S. ur Rehman, M. Siddiq, Z. Ge and S. Liu, *J. Mater. Chem. B*, 2014, **2**, 1813–1824.
120 U. Till, L. Gibot, P. Vicendo, M.-P. Rols, M. Gaucher, F. Violleau and A.-F. Mingotaud, *RSC Adv.*, 2016, **6**, 69984–69998.
121 Y. Jiang, H. Lu, Y. Y. Khine, A. Dag and M. H. Stenzel, *Biomacromolecules*, 2014, **15**, 4195–4205.
122 W. Rao, H. Wang, J. Han, S. Zhao, J. Dumbleton, P. Agarwal, W. Zhang, G. Zhao, J. Yu, D. L. Zynger, X. Lu and X. He, *ACS Nano*, 2015, **9**, 5725–5740.
123 H. Lu, B. M. Blunden, W. Scarano, M. Lu and M. H. Stenzel, *Acta Biomater.*, 2016, **32**, 68–76.
124 A. W. Du, H. Lu and M. Stenzel, *Biomacromolecules*, 2015, **16**, 1470–1479.
125 Y. Zhang, P. Lundberg, M. Diether, C. Porsch, C. Janson, N. A. Lynd, C. Ducani, M. Malkoch, E. Malmstrom, C. J. Hawker and A. M. Nystrom, *J. Mater. Chem. B*, 2015, **3**, 2472–2486.
126 S. M. Sagnella, H. Duong, A. MacMillan, C. Boyer, R. Whan, J. A. McCarroll, T. P. Davis and M. Kavallaris, *Biomacromolecules*, 2014, **15**, 262–275.
127 X. Han, R. Gelein, N. Corson, P. Wade-Mercer, J. Jiang, P. Biswas, J. N. Finkelstein, A. Elder and G. Oberdörster, *Toxicology*, 2011, **287**, 99–104.
128 R. Scherließ, *Int. J. Pharm.*, 2011, **411**, 98–105.
129 J. Friedrich, W. Eder, J. Castaneda, M. Doss, E. Huber, R. Ebner and L. A. Kunz-Schughart, *J. Biomol. Screening*, 2007, **12**, 925–937.

130 M. Zanoni, F. Piccinini, C. Arienti, A. Zamagni, S. Santi, R. Polico, A. Bevilacqua and A. Tesei, *Sci. Rep.*, 2016, **6**, 19103.
131 M. Han, Y. Bae, N. Nishiyama, K. Miyata, M. Oba and K. Kataoka, *J. Controlled Release*, 2007, **121**, 38–48.
132 I. Vermes, C. Haanen, H. Steffens-Nakken and C. Reutellingsperger, *J. Immunol. Methods*, 1995, **184**, 39–51.
133 H.-J. Li, J.-Z. Du, J. Liu, X.-J. Du, S. Shen, Y.-H. Zhu, X. Wang, X. Ye, S. Nie and J. Wang, *ACS Nano*, 2016, **10**, 6753–6761.
134 H.-J. Li, J.-Z. Du, X.-J. Du, C.-F. Xu, C.-Y. Sun, H.-X. Wang, Z.-T. Cao, X.-Z. Yang, Y.-H. Zhu, S. Nie and J. Wang, *Proc. Natl. Acad. Sci. U. S. A.*, 2016, **113**, 4164–4169.
135 K. Kyrylkova, S. Kyryachenko, M. Leid and C. Kioussi, *Methods Mol. Biol.*, 2012, **887**, 41–47.
136 F. Perche and V. P. Torchilin, *J. Controlled Release*, 2012, **164**, 95–102.
137 R. I. Dmitriev, S. M. Borisov, H. Düssmann, S. Sun, B. J. Müller, J. Prehn, V. P. Baklaushev, I. Klimant and D. B. Papkovsky, *ACS Nano*, 2015, **9**, 5275–5288.
138 W. Ke, J. Li, K. Zhao, Z. Zha, Y. Han, Y. Wang, W. Yin, P. Zhang and Z. Ge, *Biomacromolecules*, 2016, **17**, 3268–3276.
139 A. S. Mikhail, S. Eetezadi, S. N. Ekdawi, J. Stewart and C. Allen, *Int. J. Pharm.*, 2014, **464**, 168–177.
140 F. Helmchen and W. Denk, *Nat. Methods*, 2005, **2**, 932–940.
141 M. Cantisani, D. Guarnieri, M. Biondi, V. Belli, M. Profeta, L. Raiola and P. A. Netti, *Colloids Surf., B*, 2015, **135**, 707–716.
142 P. J. Verveer, J. Swoger, F. Pampaloni, K. Greger, M. Marcello and E. H. K. Stelzer, *Nat. Methods*, 2007, **4**, 311–313.
143 E. H. K. Stelzer, *Nat. Methods*, 2015, **12**, 23–26.
144 M. Mickoleit, B. Schmid, M. Weber, F. O. Fahrbach, S. Hombach, S. Reischauer and J. Huisken, *Nat. Methods*, 2014, **11**, 919–922.
145 Q. Fu, B. L. Martin, D. Q. Matus and L. Gao, *Nat. Commun.*, 2016, **7**, 11088.
146 A. Yuan, B. Yang, J. Wu, Y. Hu and X. Ming, *Acta Biomater.*, 2015, **21**, 63–73.
147 J. Zhao, H. Lu, P. Xiao and M. H. Stenzel, *ACS Appl. Mater. Interfaces*, 2016, **8**, 16622–16630.
148 R. Akasov, T. Borodina, E. Zaytseva, A. Sumina, T. Bukreeva, S. Burov and E. Markvicheva, *ACS Appl. Mater. Interfaces*, 2015, **7**, 16581–16589.
149 C. L. Waite and C. M. Roth, *Bioconjugate Chem.*, 2009, **20**, 1908–1916.
150 C. L. Waite and C. M. Roth, *Biotechnol. Bioeng.*, 2011, **108**, 2999–3008.
151 X. Liu, M. Wu, Q. Hu, H. Bai, S. Zhang, Y. Shen, G. Tang and Y. Ping, *ACS Nano*, 2016, **10**, 11385–11396.
152 V. H. B. Ho, N. K. H. Slater and R. Chen, *Biomaterials*, 2011, **32**, 2953–2958.
153 X. Zhen, X. Wang, C. Xie, W. Wu and X. Jiang, *Biomaterials*, 2013, **34**, 1372–1382.
154 X. Zhen, X. Wang, C. Yang, Q. Liu, W. Wu, B. Liu and X. Jiang, *Macromol. Biosci.*, 2014, **14**, 1149–1159.
155 C. Xie, P. Zhang, Z. Zhang, C. Yang, J. Zhang, W. Wu and X. Jiang, *Nanoscale*, 2015, **7**, 12572–12580.
156 M. Oishi, A. Tamura, T. Nakamura and Y. Nagasaki, *Adv. Funct. Mater.*, 2009, **19**, 827–834.
157 J. Zhao, H. Lai, H. Lu, C. Barner-Kowollik, M. H. Stenzel and P. Xiao, *Biomacromolecules*, 2016, **17**, 2946–2955.
158 S. E. A. Gratton, P. A. Ropp, P. D. Pohlhaus, J. C. Luft, V. J. Madden, M. E. Napier and J. M. DeSimone, *Proc. Natl. Acad. Sci. U. S. A.*, 2008, **105**, 11613–11618.
159 L. Tang, X. Yang, Q. Yin, K. Cai, H. Wang, I. Chaudhury, C. Yao, Q. Zhou, M. Kwon, J. A. Hartman, I. T. Dobrucki, L. W. Dobrucki, L. B. Borst, S. Lezmi, W. G. Helferich, A. L. Ferguson, T. M. Fan and J. Cheng, *Proc. Natl. Acad. Sci. U. S. A.*, 2014, **111**, 15344–15349.
160 S. D. Perrault, C. Walkey, T. Jennings, H. C. Fischer and W. C. W. Chan, *Nano Lett.*, 2009, **9**, 1909–1915.
161 H. S. Choi, W. Liu, F. Liu, K. Nasr, P. Misra, M. G. Bawendi and J. V. Frangioni, *Nat. Nanotechnol.*, 2010, **5**, 42–47.
162 H. Cabral, Y. Matsumoto, K. Mizuno, Q. Chen, M. Murakami, M. Kimura, Y. Terada, M. R. Kano, K. Miyazono, M. Uesaka, N. Nishiyama and K. Kataoka, *Nat. Nanotechnol.*, 2011, **6**, 815–823.
163 Y. Geng, P. Dalhaimer, S. Cai, R. Tsai, M. Tewari, T. Minko and D. E. Discher, *Nat. Nanotechnol.*, 2007, **2**, 249–255.
164 A. Theumer, C. Gräfe, F. Bähring, C. Bergemann, A. Hochhaus and J. H. Clement, *J. Magn. Magn. Mater.*, 2015, **380**, 27–33.
165 B. Kim, G. Han, B. J. Toley, C.-k. Kim, V. M. Rotello and N. S. Forbes, *Nat. Nanotechnol.*, 2010, **5**, 465–472.
166 V. P. Torchilin, *Nat. Rev. Drug Discovery*, 2014, **13**, 813–827.
167 R. Savic, L. Luo, A. Eisenberg and D. Maysinger, *Science*, 2003, **300**, 615–618.
168 T. R. Daniels, E. Bernabeu, J. A. Rodríguez, S. Patel, M. Kozman, D. A. Chiappetta, E. Holler, J. Y. Ljubimova, G. Helguera and M. L. Penichet, *Biochim. Biophys. Acta*, 2012, **1820**, 291–317.
169 S. Mishra, P. Webster and M. E. Davis, *Eur. J. Cell Biol.*, 2004, **83**, 97–111.
170 J. E. Visvader and G. J. Lindeman, *Nat. Rev. Cancer*, 2008, **8**, 755–768.
171 D. Sobot, S. Mura and P. Couvreur, *J. Mater. Chem. B*, 2016, **4**, 5078–5100.
172 S. Chuthapisith, J. Eremin, M. El-Sheemey and O. Eremin, *Surg. Oncol.*, 2010, **19**, 27–32.
173 I. K. Guttilla, K. N. Phoenix, X. Hong, J. S. Tirnauer, K. P. Claffey and B. A. White, *Breast Cancer Res. Treat.*, 2012, **132**, 75–85.
174 T. A. Elbayoumi and V. P. Torchilin, *Eur. J. Nucl. Med. Mol. Imaging*, 2006, **33**, 1196–1205.

175 V. P. Torchilin, L. Z. Iakoubov and Z. Estrov, *Trends Immunol.*, 2001, **22**, 424–427.
176 M. Munz, P. A. Baeuerle and O. Gires, *Cancer Res.*, 2009, **69**, 5627–5629.
177 F. Danhier, A. Le Breton and V. Préat, *Mol. Pharmaceutics*, 2012, **9**, 2961–2973.
178 T. Teesalu, K. N. Sugahara and E. Ruoslahti, *Front. Oncol.*, 2013, **3**, 216–224.
179 B. Leader, Q. J. Baca and D. E. Golan, *Nat. Rev. Drug Discovery*, 2008, **7**, 21–39.
180 D. A. Braasch, Z. Paroo, A. Constantinescu, G. Ren, O. K. Oz, R. P. Mason and D. R. Corey, *Bioorg. Med. Chem. Lett.*, 2004, **14**, 1139–1143.
181 R. Liu, D. M. Gilmore, K. A. Zubris, X. Xu, P. J. Catalano, R. F. Padera, M. W. Grinstaff and Y. L. Colson, *Biomaterials*, 2013, **34**, 1810–1819.
182 V. M. Le, M. D. Lang, W. B. Shi and J. W. Liu, *Artif. Cells, Nanomed., Biotechnol.*, 2016, **44**, 540–544.
183 X. Xu, C. R. Sabanayagam, D. A. Harrington, M. C. Farach-Carson and X. Jia, *Biomaterials*, 2014, **35**, 3319–3330.
184 V. B. Lokeshwar, D. Rubinowicz, G. L. Schroeder, E. Forgacs, J. D. Minna, N. L. Block, M. Nadji and B. L. Lokeshwar, *J. Biol. Chem.*, 2001, **276**, 11922–11932.
185 A. Albanese, A. K. Lam, E. A. Sykes, J. V. Rocheleau and W. C. Chan, *Nat. Commun.*, 2013, **4**, 2718.
186 K. Shin, B. S. Klosterhoff and B. Han, *Mol. Pharmaceutics*, 2016, **13**, 2214–2223.
187 C. S. Shin, B. Kwak, B. Han and K. Park, *Mol. Pharmaceutics*, 2013, **10**, 2167–2175.
188 L. Miao, J. M. Newby, C. M. Lin, L. Zhang, F. Xu, W. Y. Kim, M. G. Forest, S. K. Lai, M. I. Milowsky, S. E. Wobker and L. Huang, *ACS Nano*, 2016, **10**, 9243–9258.
189 B. Kwak, A. Ozcelikkale, C. S. Shin, K. Park and B. Han, *J. Controlled Release*, 2014, **194**, 157–167.
190 R. K. P. Benninger and D. W. Piston, *Curr. Protoc. Cell Biol.*, 2013, **59**, 4.11.1–4.11.24.
191 F. Pampaloni, N. Ansari and E. H. K. Stelzer, *Cell Tissue Res.*, 2013, **352**, 161–177.
192 C. Lorenzo, C. Frongia, R. Jorand, J. Fehrenbach, P. Weiss, A. Maandhui, G. Gay, B. Ducommun and V. Lobjois, *Cell Div.*, 2011, **6**, 22.